2000

Finite element modeling of MOI for NDE applications

Chao Chen
Iowa State University

Finite element modeling of MOI for NDE applications

Chao Chen

Major Professor: Lalita Udpa

Iowa State University

Magneto-optic eddy current imaging (MOI) systems have shown considerable promise in detecting both surface and subsurface corrosion and cracking of aging aircraft. MOI systems can produce real-time analog images of inspected parts, image both surface breaking and subsurface cracks without removing paint or decal. The images are easy to interpret, which in turn reduces inspection time and labor. Improvements and innovations in probe design are constantly required for detecting smaller and smaller flaws in complex multi-layer aircraft structures. Crucial for such studies is the development of a numerical model for simulating the underlying physical process, which can help in making more informed design optimization decisions. This thesis presents the development of a FEM for predicting quantitative values of the fields detected using MO imaging systems. The model is used extensively to study the effect of parametric variations on the field values. The results demonstrate the usefulness of the finite element model not only in understanding the capabilities of the instrument, but also in identifying optimal test parameters, and development of image interpretation algorithms.

Finite element modeling of MOI for NDE applications

By

Chao Chen

A thesis submitted to the graduate faculty
In partial fulfillment of the requirements for the degree of
MASTER OF SCIENCE

Major: Electrical Engineering
Major Professor: Lalita Udpa

Iowa State University
Ames, Iowa
2000

Graduate College

Iowa State University

This is to certify that the Master's thesis of

Chao Chen

has met the thesis requirements of Iowa State University

Major Professor

For the Major Program

For the Graduate College

TABLE OF CONTENTS

ACKNOWLEDGEMENTS

I would like to express my sincere appreciation to my major professor Dr. Lalita Udpa for her guidance and support during my graduate study. Her insight, knowledge, and kindness make my graduate study successful and happy.

I would also sincerely thank to Dr. Satish Udpa, Dr. William Lord, Dr. Yushi Sun and Dr. Paul Sacks for their support and encouragement.

I would like to thank all the members of MARG group for their friendship and help.

I would particularly like to express my thanks to my wife for her love and encouragement.

Particularly, I would like to thank Drs. W. C. L. Shih, G. L. Fitzpatrick, PRI, Inc. for their collaborations and the many discussions of the results in this thesis.

This thesis is based on the work performed at the FAA Center for Aviation Systems Reliability operated by Iowa State University and supported by the Federal Aviation Administration under Grant No. 93-G-018.

ABSTRACT

Magneto-optic eddy current imaging (MOI) systems have shown considerable promise in detecting both surface and subsurface corrosion and cracking of aging aircraft. MOI systems can produce real-time analog images of inspected parts, image both surface breaking and subsurface cracks without removing paint or decal. The images are easy to interpret, which in turn reduces inspection time and labor. Improvements and innovations in probe design are constantly required for detecting smaller and smaller flaws in complex multi-layer aircraft structures. Crucial for such studies is the development of a numerical model for simulating the underlying physical process, which can help in making more informed design optimization decisions. This thesis presents the development of a FEM for predicting quantitative values of the fields detected using MO imaging systems. The model is used extensively to study the effect of parametric variations on the field values. The results demonstrate the usefulness of the finite element model not only in understanding the capabilities of the instrument, but also in identifying optimal test parameters, and development of image interpretation algorithms.

CHAPTER 1. INTRODUCTION

The convenience of high speed transportation attracts more and more passengers to travel long distances by aircraft. However, one small error or oversight in air transportation can result in disastrous consequences. Although accident rates are very low in air transportation, once an accident occurs, the loss of human life and property is typically massive. Hence the safety of air transportation is a major concern to the aviation industry and the traveler.

Causes of aircraft accidents are numerous, such as failure of equipment and parts, environment, pilot error, air traffic control, other aircraft, fatigue cracks etc [1]. One of the most common causes, however, is the failure of equipment, particularly in the case of aging aircraft.

After Aloha Airlines B-737-200 lost part of its front fuselage during a flight in Hawaii, ten years ago, the problem of aging aircraft inspection has become a national issue. The growing concern about aging aircraft was further reinforced by a series of incidents including the crash of the TWA-800 in 1996.

Aircraft are designed for a certain life span, service and durability. However, continued growth in air travel has encouraged airlines to keep planes in service for much longer periods, frequently exceeding their original designed lives. Of the more than 3,700 U.S. commercial airplanes, one in every three is over 20 years old. In the USAF alone, thousands of aircraft have been in service over 20 years, and hundreds of these are experiencing service greater than 30 years. As aircraft service lives are extended, the need to determine the risk of flying aging aircraft with respect to fatigue cracking is critical for flight safety [1].

According to the FAA's requirement, aircraft need periodic inspection. Thousands of fasteners and bonded joints on each aircraft should be inspected and in order to handle the huge task, fast, accurate and cost effective inspection methods are clearly needed.

1.1 Traditional Nondestructive Testing Methods

Nondestructive testing (NDT) may be defined as the inspection of a test specimen for flaws without any physical destruction of the specimen. NDT techniques are extensively used in several industrial applications including aviation, steel, gas and nuclear power [2]. In all these applications, NDT can not only increase safety, but also reduce operational costs.

Several nondestructive inspection methods and instruments have been developed, over the years to address various applications. Some of the commonly used techniques are eddy current [3], magnetic flux leakage (MFL) [4], ultrasonic [5], and microwave methods [2]. A general setup of an NDT system is shown in Figure 1.1. An excitation transducer injects energy into a test sample. The induced energy interacts with the test sample. The response of this interaction is picked up by the receiving transducer to produce an output signal. This signal is then analyzed for deducing defect related information such as size, location, and shape of the defect. A description of some of the commonly used NDT techniques is given next.

1.11 Eddy Current Method

An eddy current probe consists of a coil excited by a low frequency time varying current. When the probe is brought close to a conducting material, eddy currents will be generated in the specimen (Faraday's law). The magnetic field produced by these eddy currents as given

by Ampere's law, opposes the field produced by the current in the probe coil. The net effect is to change the magnetic flux linking the coil, which by definition is the coil inductance.

The coil impedance is given by

$$Z = R + jX_L, \tag{1.1}$$

$$X_L = \omega L$$

$$\omega = 2\pi f$$

where Z is the coil impedance in ohms, R is the resistance of the coil in ohms, L is the self-inductance of the coil in Henry, and f is the excitation frequency in Hertz.

The coil inductance L plays an important role in the eddy current nondestructive testing. The inductance is proportional to the total magnetic flux Ψ linking the coil,

$$L = \frac{N\Psi}{I}, \tag{1.2}$$

where N is the number of turns of the coil, Ψ is the total magnetic flux in Weber (Wb), and I

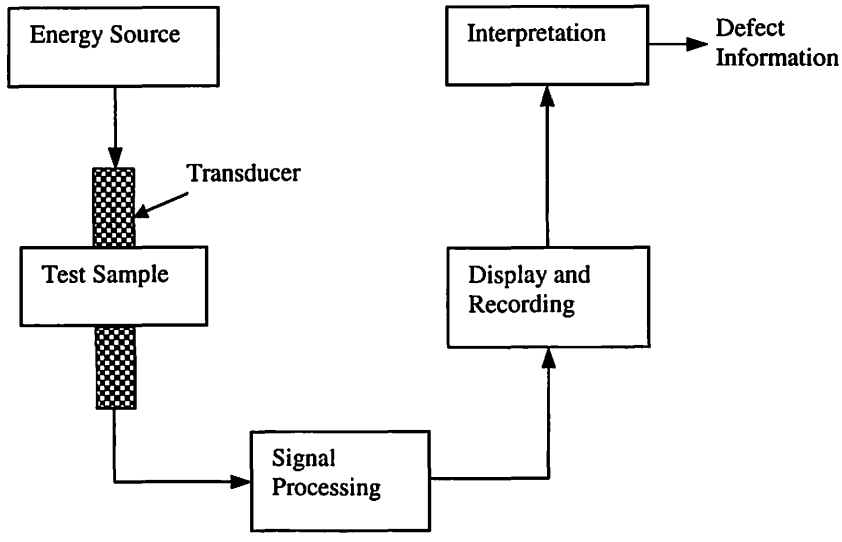

Figure 1.1 A general setup of an NDT system

is the excitation current in amperes (A). And Ψ is given by

$$\Psi = \int_s B \cdot ds \,, \tag{1.3}$$

where B is total magnetic field density.

The induced eddy currents also affect the terminal resistance of the probe coil. Defects in the specimen disturb the eddy current distribution, which in turn changes the magnetic flux. The presence of a defect is detected as a change in the terminal impedance of the probe coil, as the coil scans the surface of the specimen. Figure 1.2 shows a schematic diagram of the eddy current NDT method.

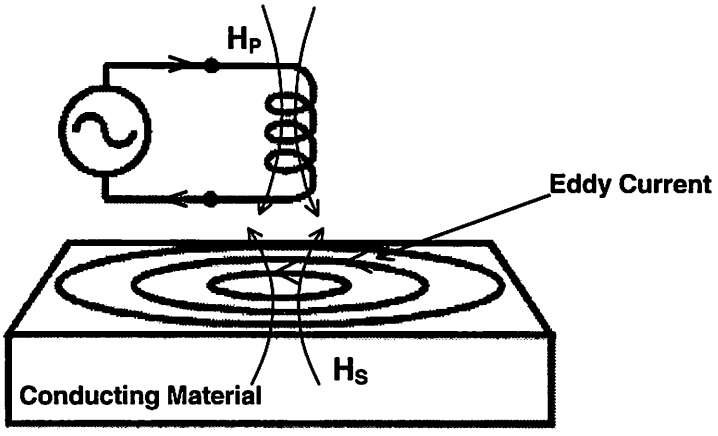

Figure 1.2 The eddy current NDT method

Eddy current methods are more suitable for detecting defects on surface or near surface, because the induced eddy currents decays as a function of depth. As an example, it can be shown that the magnitude of current density at a depth x in a metallic half plane slab excited by a plane sheet current, whose amplitude at the surface is J_0 is given by:

$$|J_x| = J_0 e^{-x/\delta} \,, \tag{1.4}$$

where the x is the depth from the surface, and δ is the skin depth. The skin depth is defined as the depth at which the field, which is generated by a uniform sheet of alternating current present on the surface of an infinite half plane of material, decays to $1/e$ of the field at the surface. The skin depth δ is decided by the frequency f, the conductivity σ, and permeability μ of the test sample. The skin depth can be calculated as [25]

$$\delta = 1/\sqrt{\pi f \sigma \mu}\,. \tag{1.5}$$

Thus, it is required to use higher frequencies for inspecting surface defects and lower frequencies for detecting the deeper embedded flaws.

An improvement of the conventional eddy current method, is provided by the pulsed eddy current method [7] which is used in the inspection of deeper subsurface structures. Since a pulse contains a broad band of frequencies, the pulsed eddy current method can obtain better resolution of both near surface and deeper structures than that obtained in single or multi-frequency inspections. The pulsed eddy current method is also limited by skin depth and is also generally classified as a surface defect detection technique. The eddy current technique is a non-contact method and is therefore fast and easy to implement.

1.1.2 Magnetic Flux Leakage NDE Method

The magnetic flux leakage (MFL) NDT method for magnetic samples is based on magnetizing the ferromagnetic test specimen and scanning its surface with a flux sensitive sensor. There are two types of MFL methods, namely, active and residual [8].

The active method is based on the operation of the test specimen on the initial magnetization curve while the residual method is based on its operation along the demagnetization curve. Excitation source can be either a yoke, direct or alternating excitation

current. Figure 1.3 shows the basic principles underlying active flux leakage testing. The diagram shows an end view of a square bar with a defect in its top surface. The defect is a crack whose major axis is perpendicular to the cross-section of the bar as shown in figure 1.3 (a). A direct current is introduced into the bar and the direction of flow is into the page.

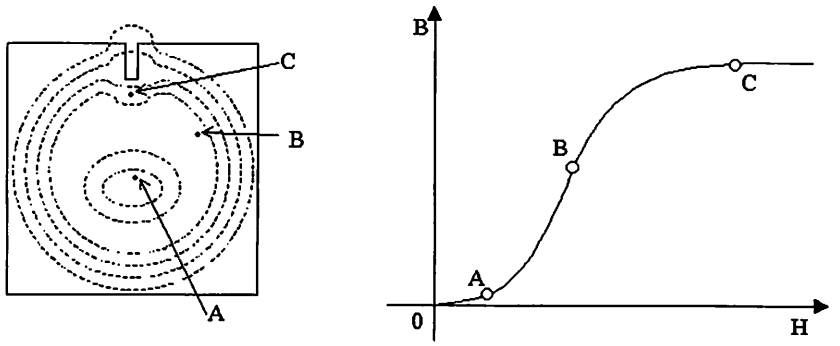

(a) (b)

Figure 1.3 Physical principles of the (a) active flux distribution and (b) initial B/H curve.

Closed magnetic lines of flux are set up encircling the current. The orientation of the lines of flux is in the clockwise direction as given by Ampere's law. The intensity of the H field changes from zero at the center of the specimen to a maximum on the surface. In the presence of the defect, the lines of flux on the upper surface get redistributed resulting in an increase of flux density just below the defect. If the current injection is sufficient, the region under the defect gets saturated decreasing its permeability. At this juncture different points of the specimen operate at different points of the magnetization curve. Since the flux lines always follow the path of least reluctance, some flux leaks into the air above the surface. The flux can be detected by using a sensor indicating the presence of the defect.

The fundamental concept of the residual MFL method is the same as that of the active MFL method except for two significant differences. The material operates along the demagnetization curve rather that the initial magnetization curve. The second difference is the current density J has to be reduced such that the regions that are far removed from the surface of the defect or material, operate close to the B-axis on the corresponding B/H characteristics of the material [4][8]. This is demonstrated by Figure 1.4.

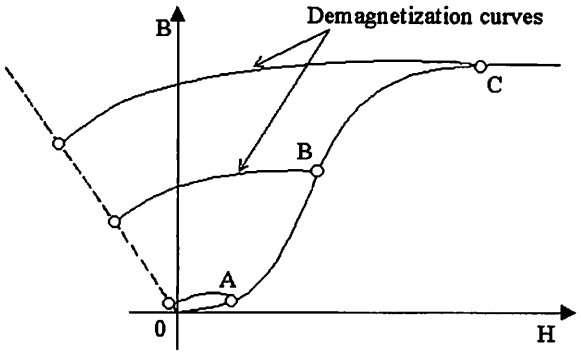

Figure 1.4 The relaxation curves of the operating points.

1.1.3 Ultrasonic Method

The ultrasonic method falls under acoustic nondestructive evaluation techniques. Generally the frequency range of the excitation used in ultrasonic NDT is above 20KHz. In this method, the ultrasonic transducer converts the input electrical pulse to an ultrasonic wave. The ultrasonic energy is coupled to the test specimen by means of a coupling medium, usually water or coupling gel. The injected wave travels through the sample and interacts with the material. The reflected or transmitted energy is measured by a pick up transducer. The

transducer converts the acoustic wave back to electrical signals. The amplitude of the received signals and the time elapsed between the incident and scattered signal can be interpreted in terms of the size and location of the flaw, respectively [5]. Figure 1.5 shows a general ultrasonic NDT system.

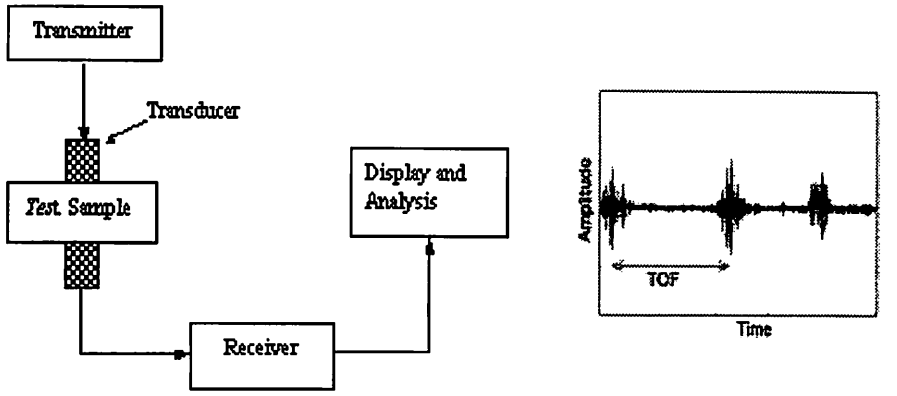

Figure 1.5 A general ultrasonic NDT system

The ultrasonic data are displayed in three possible modes. The simplest A-scan signal is obtained by fixing the ultrasonic transducer position over the surface of the test specimen and plotting the transducer response as a function of time. The time of flight (TOF) of the reflected signal indicates the flaw location. The B-scan gives the cross-section view of the flaw distribution by moving the transducer linearly over the surface of a sample under test and placing the A-scans next to each other. The C-scan provides an image of the peak amplitude of the A-scan signal in each position of the transducer as it performs a raster scan. The intensity image is mapped on the test sample by synchronizing the position of the spot on the display screen with the transducer position [9].

1.1.4 Microwave Method

Microwaves are very high frequency (0.3GHz~100GHz) electromagnetic fields, which can be concentrated into beams and propagated through space. Different materials interact differently with microwaves. When a microwave pulse strikes a conducting material, it will be reflected. In dielectric materials, microwaves are subject to rotations, phase shifts, and attenuation due to dielectric hysteresis losses [8]. The presence of a discontinuity in dielectric materials will change the response signal significantly, which means that the microwave response signals can be used to detect the defects in dielectric materials, composites and then non-conducting materials.

The advantage of microwave methods are that they can penetrate deep into nonconducting test samples, and can therefore be used to detect subsurface defects.

1.2 Problem Statement

Conventional eddy current inspections are used widely in various NDT applications. However, these methods encounter significant challenges in the inspection of aircraft structures. Due to the complex geometry of aircraft, fatigue cracks and corrosion in second and third layers of multi-layer structures are difficult to detect. Use of lower frequencies for better depth of penetration will reduce the resolution, and also increase detection difficulty. Other challenging problems are cracks under fasteners (CUFs) and multi-site damage. The detection of CUFs using conventional eddy current methods is difficult because fasteners and the fastener holes will disturb eddy current distribution and generate their own signatures. Typically the contribution from CUFs is overwhelmed by the fastener response. It is even more difficult when the fasteners are made of ferromagnetic materials. In addition, liftoff

variations produced by difference in paint thickness or surface roughness can cause false alarms.

Another challenge in aging aircraft inspection is detection of subsurface corrosion. There are many types of corrosion in aircraft skin structures, such as chemical erosion, galvanic, fretting, etc. Each type of corrosion occurs at different locations and develops in different ways.

When the aircraft, constructed of many layers of metal, is exposed to a corrosive environment, such as exhaust gases, moisture, waste water, and spillage, all factors necessary for chemical or galvanic action are present. Since some areas of the aircraft are exposed to more corrosive contaminants than others, the necessary control measures vary accordingly. Corrosive attack starts on the surface of the metal. With time, the corrosion penetrates into the core. Some common areas of corrosion problems are listed below [11]:

- Structure under lavatory systems and galleys
- Structure surrounding doors, particularly landing gear doors
- Wing skin adjacent to countersunk fastener heads
- Aluminum-faced honeycomb panels used for exterior panels and floors
- Wing-to-body joint fittings
- Fuselage lower structure
- Areas having environmentally unstable materials.

Table 1.1 presents a summary of various types of the corrosion [10].

Figure 1.6 shows the geometry of the crack under fastener (CUF). Cracks emanate from fastener holes when the rivets are punched into the rivet holes or after an extended period of

Table 1.1 Types of corrosion and their description [10]

Corrosion Type	Description
Uniform chemical attack	The simplest and most common form of corrosion, this corrosion generally produces large area of damage
Erosion	Occurs in the presence of fast moving fluid, and has a rate of attack that is much faster than corrosion from still or slow moving sources. This corrosion is most common in propellers and turbine engine components.
Galvanic	Metals of different electrochemical potential that are in contact with each other cause galvanic corrosion. The corrosion occurs at the interface between two dissimilar metals.
Pitting	Strongly localized attack produces pitting damage in the are of attack. Pitting is very common in metals with protective oxide films on them.
Crevice	Occurs when a corrosive liquid gains access to crevices in, or between components. This situation occurs frequently in lap splices. It is very similar to pitting corrosion in many respects.
Intergranular &Exfoliation	Occurs in the grain boundary regions in a polycrystalline metal. This can cause the grains to dislodge. Rolled or extruded metals with flattened grains can exhibit exfoliation, which is a severe form of intergranular corrosion.
Filiform	Has characteristics of both pitting and intergranular corrosion. The corrosion is often found in clad aluminum alloy, where an initial pit will penetrate the cladding, and then spread between the grains.
Fretting	Vibratory motion between contacting surfaces can cause material loss due to both wear and corrosion. This type of loss can be serious, since fretting conditions can cause fatigues at very low stresses.
Microbiological	Microbiological organisms can cause extensive corrosion in certain environments. The most common areas where biological corrosion occurs are in fuel tanks.
Stress Corrosion Cracking	Components that are under sustained tensile stress in corrosive environments can experience this sort of corrosion damage.

service. CUF is one of the major sources of failures.

If there are cracks under adjacent fasteners, the cracks may continue to spread rapidly, leading to uncontrolled depressurization and structure failure. This situation is known as multi-site damage (MSD). MSD occurs when stress factors are fairly uniform, so that small cracks appear and grow at roughly the same rate. Each individual crack is difficult to see and by itself poses little problem. However, the small cracks can join together quickly to form a large crack [1]. The Aloha accident was caused by multi-site damage.

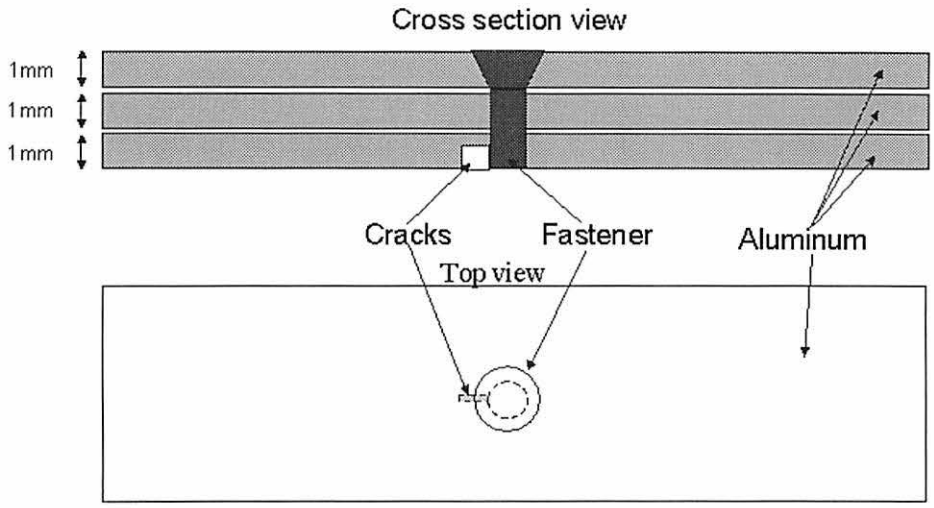

Figure 1.6 Cracks under fasteners in multi-layer structures

Conventional eddy current methods of aging aircraft inspection are time consuming due to the small probe size and large inspection area. Further, the operators need to scan the aircraft surface at the same time while they observe the signals on eddy current scopes and interpret the impedance signals. The scanning of large sample areas is labor-intensive work and requires trained operators for data interpretation.

The development of new probes and techniques for rapid and accurate inspection of these structures is of considerable interest to the aviation industry.

1.3 Magneto-Optic Imaging

The Magneto-Optic/Eddy Current Imager (MOI) is a relatively recent technique developed [13] for the inspection of aging aircraft. Magneto-optic imaging, a relatively new NDT sensor application, is based on bubble memory technology and produces easy-to-interpret, real-time analog images.

MOI uses a magneto-optic (MO) sensor to produce analog images of magnetic flux leakage from surface and subsurface defects. The flux leakage is produced using eddy current induction techniques in nonferrous metals and magnetic yokes in the case of ferromagnetic materials [14][15].

The technique has shown considerable promise in detecting corrosion and multi-layer cracking. A major advantage of the inspection method is large area coverage, accuracy, and easy-to-interpret images produced by the MOI systems.

Improvements and innovations in the MOI instrument design are constantly required for detecting smaller and smaller subsurface cracks and corrosion. Critical to the instrument's capability in detecting the relatively weak magnetic fields associated with subsurface defects is the sensitivity of the magneto-optic sensor.

In the MOI method, what we see is a qualitative image of the defect. In order to improve the sensitivity of the sensor to smaller, deeper cracks in complex aircraft structures, we need a quantitative measure of the fields produced by induced eddy currents. Using finite-element techniques to solve Maxwell's equations numerically, in conjunction with MOI observations,

it is possible to gain greater understanding of the capabilities of the instrument. This knowledge offers an understanding of the sensor requirements for different inspection needs, thereby providing a rational basis for making further sensor improvements.

1.4 Scope of the Thesis

This thesis presents the development of a finite element model (FEM) for predicting quantitative values of the fields under different parametric conditions. Chapter 2 introduces the operational principles and design of the magneto-optic/eddy current imaging systems. Chapter 3 describes the theoretical development of the finite element model for simulating the MOI phenomenon. Chapter 4 presents the simulation results obtained using the finite element model. Validation of the model with experimental measurements and various parametric studies are discussed in this chapter. Chapter 5 presents a summary and some directions for future research.

CHAPTER 2. MAGNETO-OPTIC/EDDY CURRENT IMAGING

2.1 Introduction

The magneto-optic/eddy current imaging technique is a relatively new method, which has shown significant promise in detecting subsurface cracks and corrosion in aircraft skin structures. The principles of the magneto-optic imaging are based on Faraday electromagnetic induction and the Faraday rotation effect. Using principles of electromagnetic induction, eddy currents are induced into the conducting test samples. The Faraday rotation effect is exploited in the detection of magnetic flux associated with defects in the sample. A schematic of the MOI instrument is shown in Figure 2.1. A copper foil is used to produce uniform sheet currents at low frequency (1.5-100kHz), which induce eddy currents in the conducting test specimen. Under normal conditions, the associated magnetic flux is tangential to the specimen surface. Cracks in the specimen cause the eddy currents to bend, generating a normal component of the magnetic flux density. This leakage magnetic field is then imaged using the Faraday rotation effect. A linearly polarized light is incident normally on the MO sensor placed above the copper foil. Leakage magnetic fields rotate the plane of polarization of the incident light. When the light reflected from the MO sensor is viewed through the analyzer, the local occurrence of normal magnetic flux is seen as 'dark' areas depending on the direction of the field. The basic operational principles underlying the magneto-optic/eddy current imaging are covered in the following sections [16][13].

2.2 Faraday Rotation

The Faraday rotation effect was first observed in 1845. It was observed that magnetic fields affect optical properties of certain materials so that when linearly polarized light is transmitted through the material in the direction of an applied magnetic field, the plane of polarization is rotated (Figure 2.2). This is the Faraday magneto-optic effect, also referred to as the Faraday rotation, where the amount of rotation is proportional to the magnetic field H and the path length *l*.

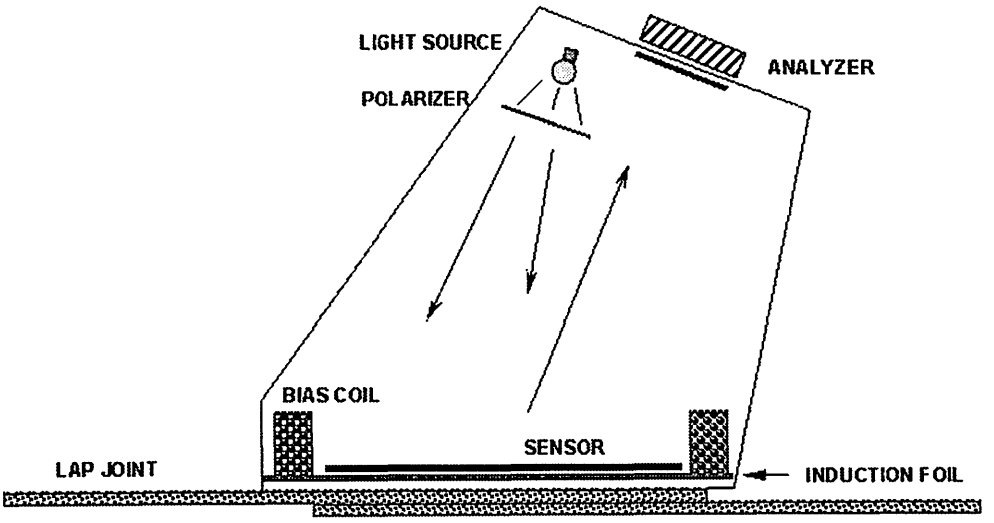

Figure 2.1 Schematic of the magneto-optic/eddy current imaging device [17].

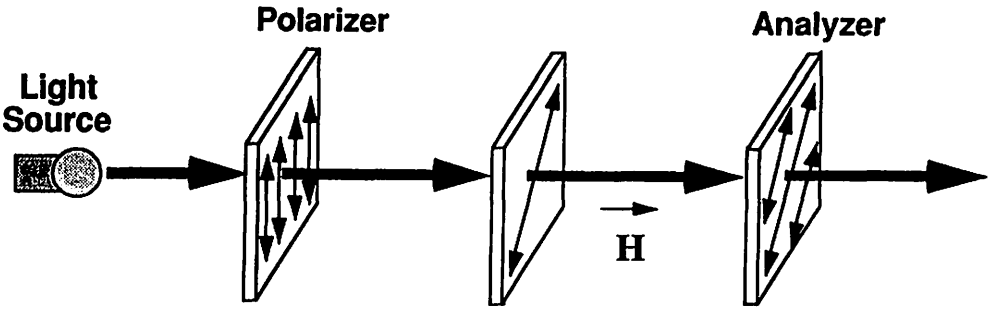

Figure 2.2 Faraday rotation effect

Figure 2.2 Faraday rotation effect

Recent years have seen an increasing interest in the Faraday rotation effect largely due to its application in the design of antennas, high-density data storage, and NDE systems. In the next section, we discuss the physics of the Faraday rotation, and its application to magneto-optic/eddy current systems.

2.3 Macroscopic Description of Magneto-Optic Effects

The magneto-optic interactions at a macroscopic level can be explained by solving Maxwell's equations combined with appropriate material equations. These interactions may be characterized by the constitutive relations [18],

$$\mathbf{D} = [\varepsilon]\mathbf{E}. \tag{2.1}$$

and

$$\mathbf{B} = [\mu]\mathbf{H}. \tag{2.2}$$

where **D** is the electric displacement, **E** is the electric field strength, **B** is the magnetic flux density, **H** is the magnetic field strength, $[\varepsilon]$ is the complex permittivity tensor of the medium, and $[\mu]$ is the permeability tensor of the medium. Equations 2.1 and 2.2 describe how materials respond to the electromagnetic fields **E** and **H** of the incident radiation.

If the magnetization is in the z-direction, a rotation about the z-axis should leave the relationship (Equation 2.2) between **B** and **H** unchanged, and, in the rotated frame we have

$$\mathbf{B}' = [\mu]\mathbf{H}'. \tag{2.3}$$

For a rotation angle θ, any vector **r** in the original frame is transformed to r′

$$\mathbf{r}' = [\mathbf{R}]\mathbf{r}. \tag{2.4}$$

where [**R**] is the rotation matrix operator given by,

$$[\mathbf{R}] = \begin{bmatrix} \cos\theta & \sin\theta & 0 \\ -\sin\theta & \cos\theta & 0 \\ 0 & 0 & 0 \end{bmatrix}. \tag{2.5}$$

When Equation 2.4 is applied to both sides of Equation 2.3 and the result compared with Equation 2.1, we see that the permeability tensor must satisfy the condition

$$[\mu] = [\mathbf{R}]^{-1}[\mu][\mathbf{R}]. \tag{2.6}$$

and must have the skew-symmetric form

$$[\mu] = \begin{bmatrix} \mu_{11} & \mu_{12} & 0 \\ -\mu_{12} & \mu_{11} & 0 \\ 0 & 0 & \mu_{33} \end{bmatrix}. \tag{2.7}$$

or in more specific terms

$$[\mu] = \mu_0 n^2 \begin{bmatrix} 1+FQ^2 & -iQ & 0 \\ iQ & 1+FQ^2 & 0 \\ 0 & 0 & 1 \end{bmatrix}. \tag{2.8}$$

where, n is the refractive index of the demagnetized (Q=0) isotropic material, Q the primary magneto-optic constant proportional to the magnetization, and F is a second magneto-optic constant that becomes significant in the description of second-order ($\propto Q^2$) magneto-optic effects. Since only first-order effects will be considered, the form of the permeability tensor used here is

$$[\mu] = \begin{bmatrix} 1 & -iQ & 0 \\ iQ & 1 & 0 \\ 0 & 0 & 1 \end{bmatrix}. \tag{2.9}$$

The interaction of electromagnetic radiation with magneto-optic materials is easy to understand in terms of electromagnetic plane wave solutions of Maxwell's equations and the

appropriate material equations. Any electromagnetic field must satisfy all of Maxwell's equations,

$$\nabla \times \mathbf{E} = -\frac{\partial \mathbf{B}}{\partial t} \qquad \textit{(Faraday's law)} \tag{2.10}$$

$$\nabla \times \mathbf{H} = \mathbf{J} + \frac{\partial \mathbf{D}}{\partial t} \qquad \textit{(Ampere's law)} \tag{2.11}$$

$$\nabla \cdot \mathbf{D} = \rho \qquad \textit{(Gauss's law)} \tag{2.12}$$

$$\nabla \cdot \mathbf{B} = 0 \qquad \textit{(Gauss's law)} \tag{2.13}$$

where, **E** is the electric field strength, **B** is the magnetic flux density, **H** is the magnetic field strength, **D** is the electric displacement, **J** is the electric current density, and ρ is the electric charge density. In this problem we can assume $\rho = 0$.

Consider an electromagnetic linear plane wave in free space (charge density $\rho = 0$), propagating in the $+\hat{z}$ direction. Applying Maxwell's equations, we can derive the expressions for plane waves as

$$\mathbf{E} = (\hat{x}E_x + \hat{y}E_y)\exp[\mathrm{j}(\omega t - kz)] \tag{2.14}$$

$$\mathbf{H} = (\hat{x}H_x + \hat{y}H_y)\exp[\mathrm{j}(\omega t - kz)] \tag{2.15}$$

where ω is the angular frequency and $k = \frac{2\pi}{\lambda}$. We see that the electric and magnetic fields of the wave have only $\hat{x}$ and $\hat{y}$ components.

Substituting Equation 2.14 in Equation 2.10, we get

$$E_x = vB_y, \; E_y = -vB_x, \tag{2.16}$$

and from Equations 2.15 and 2.11, we can get

$$H_x = -vD_y, \; H_y = vD_x \tag{2.17}$$

where $v = \omega / k$.

Applying these to Equation 2.1 and 2.2 we get,

$$\frac{H_y}{H_x} = \frac{-jv^2 Q\varepsilon_0}{1 - v^2\varepsilon} = \pm j \tag{2.18}$$

Hence,
$$v = \frac{\omega}{k} = \sqrt{\frac{1}{\varepsilon_0(1 \pm Q)}} \tag{2.19}$$

The wave vectors for the left and right circularly polarized waves are

$$k_L = \omega\sqrt{\varepsilon_0(1+Q)} \tag{2.20}$$

$$k_R = \omega\sqrt{\varepsilon_0(1-Q)}\,. \tag{2.21}$$

Since the propagation direction of the linear polarized light is along $+\hat{z}$ in the isotropic media at the position z = 0,

$$H = xH_0 = (\hat{x} + j\hat{y})\frac{H_0}{2} + (\hat{x} - j\hat{y})\frac{H_0}{2} \tag{2.22}$$

where the linearly polarized wave has been resolved into two orthogonal circular polarized component with $H_0 = \|H_x\| = \|H_y\|$.

After the wave goes through *d* units in the media, the magnetic field will be

$$H = (\hat{x} + j\hat{y})\frac{H_0}{2}e^{-jk_L d} + (\hat{x} - j\hat{y})\frac{H_0}{2}e^{-jk_R d} \tag{2.23}$$

where k_L and k_R are the wave vectors for the left and right circular polarized waves, respectively. Equation 2.23 can be rewritten as:

$$H = \frac{H_0}{2}(e^{-jk_L d} + e^{-jk_R d})(\hat{x} + \hat{y}j\tan\theta) \tag{2.24}$$

where $$\theta = \frac{(k_L - k_R)d}{2} \tag{2.25}$$

From the above result, we see that the wave is still linearly polarized, but the polarization axis has been rotated by an angle of θ in counterclockwise direction. This phenomenon is called Faraday Rotation.

The rotation angle θ is proportional to Q ($k = \omega\sqrt{\varepsilon_0(1 \pm Q)}$), and Q is proportional to the magnetization M. Hence we can express the rotation angle simply as

$$\theta = KMd, \tag{2.26}$$

where K is called Kundt's constant [6].

2.4 Garnet Film

The magneto-optic sensor used in the MO instrument consists of a ferromagnetic bismuth doped iron garnet film with 0.5mm thickness and 75mm diameter. These films exhibit three important properties that are useful in the operation of a practical magneto-optic/eddy current imaging device [13]. First, these films have a magnetic anisotropy property with an easy axis of magnetization normal to the sensor surface and a 'hard' axis of the magnetization in the plane of the sensor. The sensor is insensitive to the relatively large magnetic field along the 'hard' axis, but is very sensitive to the normal magnetic fields along the 'easy' axis. Second, if the magnetic fields along the easy axis are removed, the films will retain most of the established magnetization, i.e., they have *memory*. Third, the material is transparent to light and is characterized by a large value of specific Faraday rotation (rotation per unit of thickness) in the range of 20,000 to 40,000 degrees/cm of film thickness. This feature is

particularly useful in detecting low level magnetic fields, which is desirable in NDE applications.

When a linearly polarized light is transmitted through a garnet sensor film, the polarization plane of the light will be rotated by an angle θ. The angle of rotation is decided by the wave vector of the light k, the local magnetization M, path lengh d, and the specific Faraday rotation θ_f of the garnet film. If the incident light is reflected back through the sensor film again, the effective Faraday rotation angle θ is doubled since the light passes through the garnet sensor twice. Note that the quantity $k \cdot M$ will have the same sign in either direction.

When the reflected light is viewed through the analyzer, a local occurrence of the normal component of the magnetic flux is seen as a 'dark' area.

2.5 Domain Wall

In practice, the MO images are not perfect 'dark' and 'light' images. In Figure 2.3 we see the difference between the ideal model predicted image and experimental image of a circular hole. There are many thin lines randomly distributed in an experimental image. The curves actually show the structures of the serpentine domains in the sensor film.

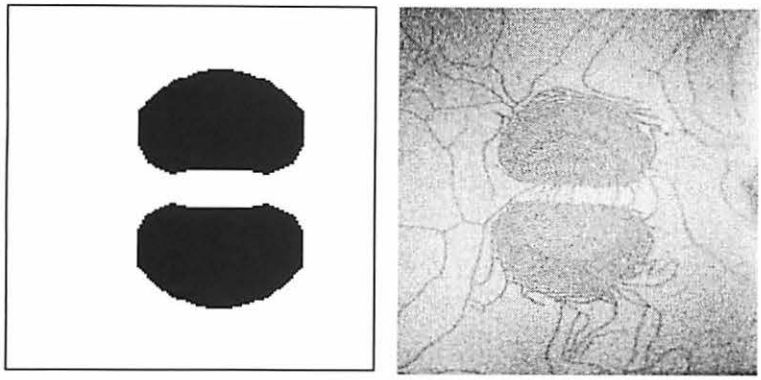

(a) (b)

Figure 2.3 (a) ideal image (b) experimental image

Magnetic materials exhibit many types of domain structures, such as bubble lattices, mazes, and strip domains. Figure 2.4 and 2.5 show some of these domain structures and the influence of external magnetic fields on the domain. The domain structures are affected by magnetic anisotropy and magnetization of the material, the sample shape, presence of defects, the external magnetic field, temperature, surface treatment, and the history of the sample [18]. Domain structures are studied extensively in bubble memory technology and used in the design of high density data storage.

(a) (b) (c)

Figure 2.4. (a) maze (b) bubble lattice (c) strip domain structure [18]

(a) (b) (c)

Figure 2.5 Maze domain structure: (a) H=0, (b) H=0.7H_s, (c) H≤H_s, where H_s is the saturation field [18].

The garnet film in MO sensor contains two kinds of domain structures, in which the magnetic moments are directed either along or opposite to the 'easy' axis. These domains are separated by domain walls. Figure 2.6 shows the (a) domain structures in a garnet film and (b) their corresponding MO images.

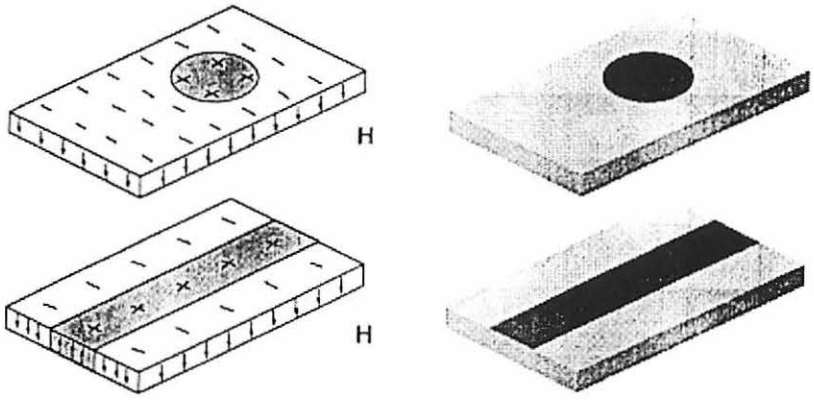

(a) (b)

Figure 2.6 (a) domain structures and (b) corresponding MO images.

When a magnetic field is applied normal to the sensor plane, the domain structures are rearranged. Domains having a magnetization direction that coincides with that of external magnetic field expand, whereas the domains with the opposite orientation shrink. When the external field reaches a critical value H_s, which is referred as the saturation field the case of a material with stripe or maze domains, the domains having magnetization oriented opposite to the external field vanish, as shown in Figure 2.5. The width of the domain is determined by the relation

$$w \approx 2.7(lh)^{1/2} \tag{2.27}$$

where $l = (4\pi M_s)^{-1}\sigma_w$ is the parameter of the material that is referred to as magnetic length, σ_w is the energy per unit area of the domain wall, M_s is the saturation magnetization, and h is the film thickness [18]. If the applied magnetic field is removed, the ferromagnetic property of the film, allows the domains to keep the current status, until another magnetic field (erase field) is applied.

Note that in magnetic films with uniaxial magnetic anisotropy, magnetic moments of the domains are generally directed in two opposite directions perpendicular to the film surface. The binary modes of the direction of magnetic moments result in producing binary valued MO images. The intensity of the magnetic field will affect the size of the domains and not the intensity of the image.

2.6 Sheet Current Excitation

The Faraday rotation effect is used for imaging the leakage magnetic fields associated with the induced eddy current in the test sample.

Practical magneto-optic/eddy current imaging instruments use a large 3-inch copper sheet to produce uniform sheet currents at low frequency (1-50kHz), which induce eddy currents in the specimen being inspected. The magnetic fields associated with the sheet currents (in both the foil and the test piece) lie parallel to the hard axis of magnetization of the sensor. These fields have little or no effect on the state of magnetization of the sensor. The copper foil carrying a time varying (sinusoidal) planar current shown in Figure 2.7(a) is used to induce eddy currents in the sample as shown in Figure 2.7(b).

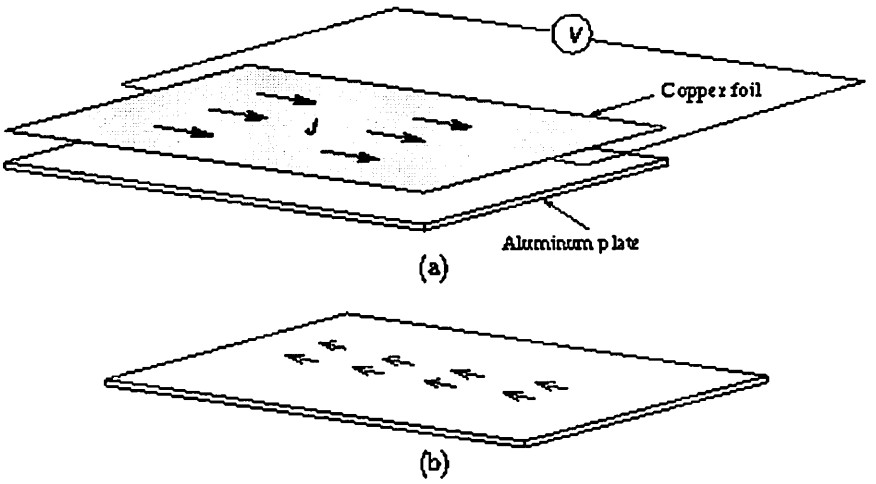

Figure 2.7 (a) The excitation current in the conducting foil (b) Induced eddy currents in a plate of conducting material [6].

2.7 Magneto-optic/eddy current imaging

The presence of defects in the sample, such as a hole, a rivet, or a crack, distorts the uniform eddy currents. The distorted eddy currents produce detectable magnetic fields normal to the surface of the test piece. Note that the normal component of the magnetic field is detected by the sensor since it lies parallel to the sensor's easy axis of magnetization. Figure 2.8 shows the current paths in the test piece and the normal component of the magnetic fields associated with the eddy currents induced in the test piece during the first and second half cycles of the eddy current. These time varying magnetic fields, which are generally associated with cracks or corrosion, are able to affect the state of magnetization of the sensor because these fields easily penetrate the thin (relative to skin depth) copper foil.

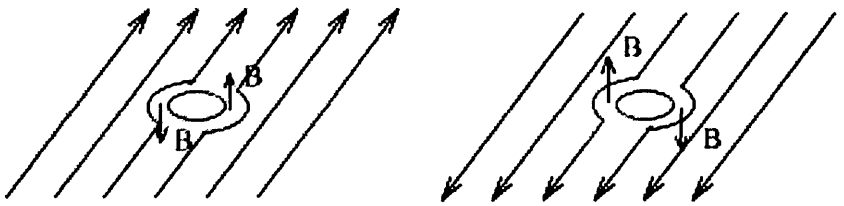

(a) (b)

Figure 2.8 Current paths in the test piece and the normal component of the magnetic fields (a) first half cycle (b) second half cycle

In addition to the application of information-carrying magnetic fields or the leakage fields at the eddy current excitation frequency, a bias coil is used to generate a low frequency bias magnetic field. Normally the flux leakage associated with the defect is much smaller than the threshold value of the magnetic field required to flip the domain in a garnet sensor film (± 3

Gauss) [17]. Setting the bias field to a value just below the threshold H_T allows the sensor to detect very small leakage fields. The resultant total magnetic field applied to the magneto-optic sensor is the sum of leakage and bias fields. From Figure 2.9, we see that only the peak values in the same direction as the bias field will exceed the threshold of the sensor film. Thus, only these peaks will be recorded by the sensor film. This is indicated by the image in Figure 2.9 (a) for the first half cycle. In the next half cycle, this condition is satisfied at y resulting in the image shown in Figure 2.9 (b). The image shown in Figure 2.9 (c) is formed at the end of a cycle.

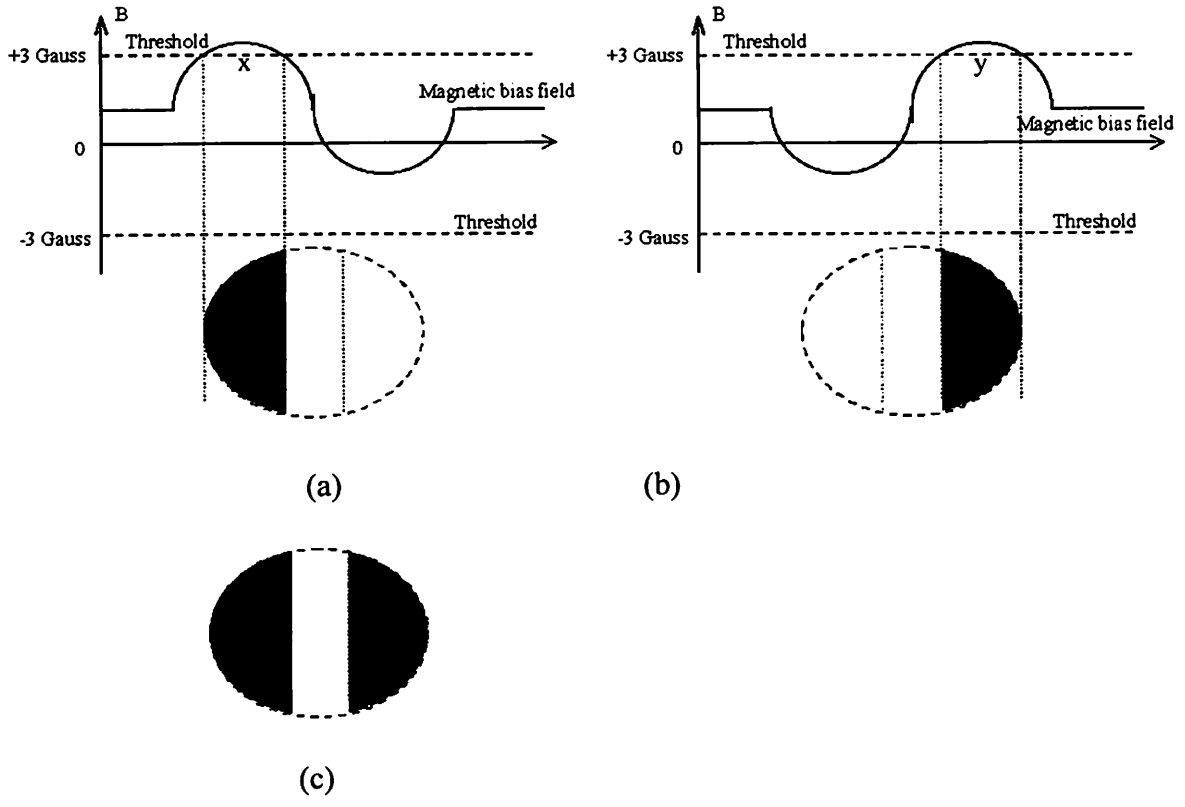

(a) (b)

(c)

Figure 2.9 The sum of leakage and bias fields and corresponding image in (a) first half cycle (b) second half cycle; (c) the image generated by the whole cycle.

Figure 2.10 shows the actual procedure for forming an image. First, an erase pulse in the bias coil generates a magnetic field in the reverse direction of the bias field. This field is large enough to clear the image and set the intensity to a uniform value. Then, the bias field and the excitation current in the foil are established at the same time. During this time period alternating currents in the foil and the static bias field are active, as indicated in Figure 2.8, and an image is recorded by the sensor film. Because one period of the alternating magnetic field is relatively shorter than the response time of the garnet film, and the field is weak. 26 cycles of the excitation current are needed to enhance the image and provide the image shown in Figure 2.9 (c). After the excitation is turned off, the image will remain on the film until next erase pulse is applied.

2.8 Multi-direction (Rotating) Eddy Current Excitation

When the crack is parallel to the direction of the linear excitation current, the conventional linear excitation MOI instrument is insensitive to the crack. A rotating current can solve this problem. Applying two separate linear excitation currents with a 90° phase difference perpendicular to each other, resultant rotating eddy currents are set up in the specimen. The current density in the testing area is expressed as

$$J = \hat{x}\, J_0 sin(wt) + \hat{y}\, J_0 cos(wt) \tag{2.28}$$

$$= J_0 \angle (wt + \tfrac{\pi}{2}),$$

where $\hat{x}$ and $\hat{y}$ are two orthogonal vectors. We must note that this current is different from that obtained using circular coil excitation, which is axisymmetric. The rotating excitation current generates a uniform field, which rotates.

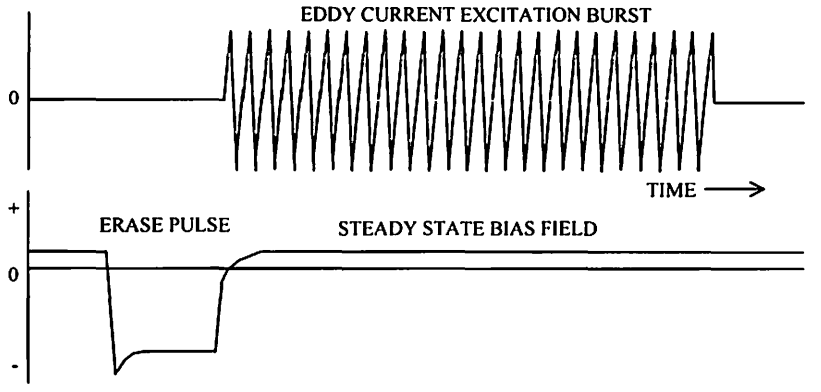

Figure 2.10 Wave form for the excitation eddy current and bias current [17].

Figure 2.11(a) shows a MO image of first-layer crack in a lap joint using linear excitation. Figure 2.11(b) shows the MO image of the same sample using rotating current excitation. In the MO image generated by linear excitation current, the crack is not detected. While with the rotating current excitation, the cracks are clearly observed in the MO image. Cracks with arbitrary orientations can thus be detected when a rotating sheet excitation current is used.

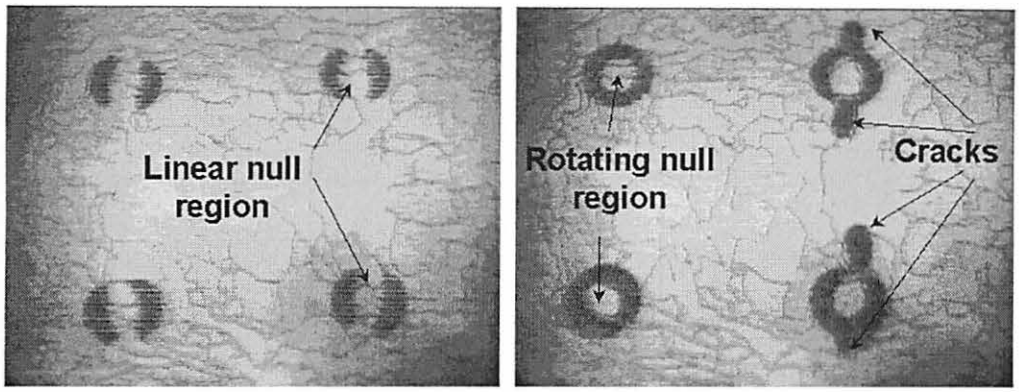

(a) (b)

Figure 2.11 (a) MOI image using linear excitation (b) MOI image using rotating excitation

2.9 Advantages of MOI

The MOI system has shown considerable promise in aging aircraft inspection. In a traditionally high-frequency eddy current application, MOI has gained favor due to the following advantages [13]:

1. An MOI system produces large area, real time, analog images of inspected parts, which makes it relatively faster than traditional methods.
2. It images both surface breaking and subsurface cracks. An MOI system can detect hidden corrosion with 10% loss of material under 1.5mm thick single layer panel, which meets current requirements. Subsurface corrosion with more than 20% loss of material can be detected by the MOI system, in a double layer sample.
3. It is easy to interpret the image, which reduces the training requirements and fatigue of the operator.
4. It eliminates need for removing paint or decal.

5. The MOI technique can be used on conducting and ferromagnetic samples as well as composites by "tagging" the sample with ferromagnetic particles

2.10 Sensor Improvement

Due to the different types of corrosion and complex skin structures of aircraft skin, the inspection is in general a challenging task. The MOI system currently meets the requirements for detecting 10% loss of material on simulated lap skins. Reliable detection of corrosion loss of material below 5% is encouraged by the aviation industry. Hence improvements in the sensor and the MOI instrument to get higher sensitivity is always desirable.

The MO sensor is the most crucial part of the MOI system. The more sensitive the sensor, the greater the probability of detection of a critical flaw. The binary MO image gives a qualitative measure of the defect and in order to improve sensor design, it is necessary to obtain a quantitative value of the leakage field. It is therefore necessary to develop a numerical model for simulating the underlying physical process, which can help in making more informed design decisions. This thesis presents the development of a numerical model based on Finite Element analysis and its application to the modeling of MO images. The model development is described in the next chapter.

CHAPTER 3. FINITE ELEMENT MODELING

3.1 Introduction

Finite element analysis is a numerical technique used for solving partial differential equations. It was first used in aircraft design in 1950s. The method has been adapted and applied extensively in other areas, such as structural analysis, fluid mechanics, nuclear engineering, and electromagnetic field analysis. Today, the finite element method has been recognized as a general method for solving engineering and mathematical problems [19].

The finite element method is based on principles of variational calculus [20]. The approach of the variational method is first to derive a functional from the governing equation which is minimized. The energy functional represents the energy of the system and its stationary value is a minimum. The minimization of the functional also gives the solution of the partial differential equation. Once the energy functional for the system is determined, the finite element formulation consists of the following steps [19]:

(i) Discretization or subdivision of the domain

(ii) Selection of the interpolation functions

(iii) Formulation of the system of equations

(iv) Solution of the system of equations.

This chapter describes the theoretical development of a Finite Element (FE) model for simulating the magneto-optic/eddy current inspection. The model can be used to predict leakage flux associated with induced currents in the presence of subsurface corrosion and cracks in multi-layer structures. The model will also serve as an experimental test bed for

carrying out parametric studies that are too expensive to perform experimentally. In addition the flux and eddy current distribution in the presence of cracks can be visualized, which in turn helps make intelligent decisions and design optimization.

3.2 Electromagnetic Field Equations

The differential equations governing the electromagnetic fields are given by the Maxwell's equations [21],

$$\nabla \times \mathbf{E} = -\frac{\partial \mathbf{B}}{\partial t} \qquad \textit{(Faraday's law)} \tag{3.1}$$

$$\nabla \times \mathbf{H} = \mathbf{J} + \frac{\partial \mathbf{D}}{\partial t} \qquad \textit{(Ampere's law)} \tag{3.2}$$

$$\nabla \cdot \mathbf{D} = \rho \qquad \textit{(Gauss's law)} \tag{3.3}$$

$$\nabla \cdot \mathbf{B} = 0 \qquad \textit{(Gauss's law)} \tag{3.4}$$

where, **E** is the electric field strength, **B** is the magnetic flux density, **H** is the magnetic field strength, **D** is the electric displacement, **J** is the electric current density, and ρ is the electric charge density. In addition, the following constitutive relations are used to describe linear and isotropic media

$$\mathbf{B} = \mu \mathbf{H} \tag{3.5}$$

$$\mathbf{D} = \varepsilon \mathbf{E}\,. \tag{3.6}$$

According to Ohm's law, the conduction current density $\mathbf{J}$, is defined as,

$$\mathbf{J} = \sigma \mathbf{E} + \mathbf{J}_s, \tag{3.7}$$

where $\mathbf{J}_s$ is the source current.

The following assumptions have been made in the model development here.

1) The media is linear and isotropic in each element, i.e., the dielectric constant, the magnetic permeability and the conductivity are single valued constants. This assumption has been

applied in the Equations 3.5, 3.6 and 3.7 for the convenience of modeling, but under special circumstances, changes in conductivity and permeability can be implemented in one element.

2) For magnetostatic problems, the displacement current in Equation 3.2 is zero. In the magneto-optic/eddy current method the frequency of excitation is of the order of few MHz. It has been shown that the displacement currents can be neglected at these frequencies for most MOI test scenarios [22].

3) Since there is no free charge in the solution region, in Equation 3.4, the electric charge density ρ is zero.

Using these assumptions, and substituting Equation 3.5 and 3.7 into Equation 3.2, we get

$$\nabla \times \frac{1}{\mu}\mathbf{B} = \sigma \mathbf{E}. \tag{3.8}$$

The magnetic flux density **B** can be expressed as the curl of the magnetic vector potential **A**.

$$\mathbf{B} = \nabla \times \mathbf{A}. \tag{3.9}$$

Substituting Equation 3.9 into Equation 3.8 yields

$$\nabla \times \frac{1}{\mu}(\nabla \times \mathbf{A}) = \sigma \mathbf{E} + \mathbf{J}_s. \tag{3.10}$$

Equation 3.9 gives the definition of the magnetic vector potential **A**. However, the divergence of the magnetic vector potential is not defined, and consequently the magnetic vector potential **A** is not uniquely defined. Since $\nabla \times \mathbf{A}$ always satisfies the $\nabla \cdot \mathbf{B} = 0$ condition, $\nabla \cdot \mathbf{A}$ can be defined in a manner that Equation 3.10 is satisfied. Thus, Equation 3.1 can be written as

$$\nabla \times \mathbf{E} = \nabla \times (-\frac{\partial \mathbf{A}}{\partial t}). \tag{3.11}$$

Integrating both side of Equation 3.11, we can get the relation between electric field strength **E** and magnetic vector potential **A**

$$\mathbf{E} = -\frac{\partial \mathbf{A}}{\partial t} - \nabla \Phi, \tag{3.12}$$

where Φ is the electric scalar potential. Substituting Equation 3.12 into Equation 3.10 yields

$$\nabla \times \frac{1}{\mu}(\nabla \times \mathbf{A}) = -\sigma \frac{\partial \mathbf{A}}{\partial t} - \sigma \nabla \Phi + \mathbf{J}_s. \tag{3.13}$$

The gradient of the electric scalar potential $\nabla \Phi$ can be set to zero in this work and hence Equation 3.13 can be written as

$$\frac{1}{\mu} \nabla \times (\nabla \times \mathbf{A}) = -\sigma \frac{\partial \mathbf{A}}{\partial t} + \mathbf{J}_s. \tag{3.14}$$

In eddy current problem, the excitation currents are single frequency alternating currents and the electromagnetic fields generated by the source currents are sinusoidal steady fields. Therefore, the derivative of the magnetic vector potential can be written as

$$\frac{\partial \mathbf{A}}{\partial t} = -j\omega \mathbf{A}. \tag{3.15}$$

and Equation 3.14 becomes

$$\frac{1}{\mu} \nabla \times (\nabla \times \mathbf{A}) = -j\omega\sigma \mathbf{A} + \mathbf{J}_s. \tag{3.16}$$

Using the vector identity $\nabla \times (\nabla \times \mathbf{A}) = \nabla(\nabla \cdot \mathbf{A}) - \nabla^2 \mathbf{A}$, and Coulomb gauge $\nabla \cdot \mathbf{A} = 0$, we obtain diffusion equation,

$$\frac{1}{\mu} \nabla^2 \mathbf{A} = j\omega\sigma \mathbf{A} - \mathbf{J}_s \tag{3.17}$$

Equations 3.16 and 3.17 are basic field equations which describe the electromagnetic fields in terms of magnetic vector potential **A** in eddy current problems. Analytical solutions of the above equation are available only in the case of very simple geometry. In the analysis of most practical, real world test and defect geometry, numerical methods are used widely for solving the equation numerically.

3.3 3D Finite Element Formulation of Electromagnetic Fields

Among the many methods available for finite element formulation, the weighted residual method (Galerkin's method) [23] and the use of energy functional based on the global energy balance concept are commonly used.

The energy balance function for the electromagnetic field problems can be written as,

$$F = \textit{magnetic field energy} + \textit{electric field energy}$$

$$= \textit{stored energy} + (\textit{dissipated energy} - \textit{input energy}). \qquad (3.18)$$

The stored energy is due to the magnetic field, the input energy is derived from the impressed current densities and the dissipated energy arises from the eddy current densities in the conducting parts of the geometry, excluding sources.

According to the field theory, the energy functional can be written as

$$F = \int_v \frac{1}{2}\boldsymbol{H}\cdot\boldsymbol{B}dv + \int_v \frac{1}{2}\boldsymbol{J}\cdot\boldsymbol{A}dv \qquad (3.19)$$

$$= \int_v \frac{1}{2}\mathbf{H}\cdot\mathbf{B}dv + \int_v \frac{1}{2}\mathbf{J}_e\cdot\mathbf{A}d - \int_v \frac{1}{2}\mathbf{J}_s\cdot\mathbf{A}dv$$

where $\mathbf{J}_s$ is the excitation source current, $\mathbf{J}_e$ is the eddy current induced by the excitation current. Substituting the relation $\mathbf{H} = \frac{1}{\mu}\mathbf{B}$ and $\mathbf{J} = \sigma\mathbf{E} = \sigma(-\frac{\partial \mathbf{A}}{\partial t} - \nabla\Phi)$ into the above equation

$$F = \iint_v [\frac{1}{2\mu}\mathbf{B}^2 + \frac{1}{2}\sigma(-\frac{\partial \mathbf{A}}{\partial t})\cdot\mathbf{A} - \mathbf{J}_s \cdot \mathbf{A}]dv . \tag{3.20}$$

For eddy current problems with single frequency harmonic excitation, $\frac{\partial \mathbf{A}}{\partial t} = j\omega\mathbf{A}$, the Equation 3.20 can be written as

$$F = \iint_v [\frac{1}{2\mu}|\nabla \times \mathbf{A}|^2 + \frac{1}{2}j\omega|\mathbf{A}|^2 - \mathbf{J}_s \cdot \mathbf{A}]dv \tag{3.21}$$

The first term in the functional represents the energy stored in the magnetic fields. The second term represents the eddy current losses in the conducting region. The third term is derived form the harmonic source current.

In three dimensions the energy functional can be expressed as

$$F = \iint_v [\frac{1}{2\mu}\{|\frac{\partial A_z}{\partial y} - \frac{\partial A_y}{\partial z}|^2 + |\frac{\partial A_x}{\partial z} - \frac{\partial A_z}{\partial x}|^2 + |\frac{\partial A_y}{\partial x} - \frac{\partial A_x}{\partial y}|^2\}$$

$$+ \frac{1}{2}j\omega\sigma(A_x^2 + A_y^2 + A_z^2) - (J_x A_x + J_y A_y + J_z A_z)]dxdydz . \tag{3.21}$$

The magnetic vector potential and current densities in the above equation are all complex quantities.

The discretization of the region of interest is a very important step in the finite element method. A solution domain with infinite degrees of freedom is replaced by a system having a

finite number of degrees of freedom by discretizing the region using finite element [19]. The geometry of the element will affect the accuracy of results and computing time.

The most commonly used element in 3D problems is the tetrahedron, triangle (prism), and hexahedrons. In this project, we used the linear hexahedral elements. The hexahedral elements have some advantages compared to other element shapes. They need fewer elements to achieve the same degree of discretization, thus resulting in less data storage and computation time for the finite element solution. Secondly, they are also easy to generate and visualize.

The discretization method also has a significant impact on the accuracy and efficiency of the model. Normally a good discretization method should satisfy the following rules [22]:

1) More nodes are used to achieve adequate accuracy in the high gradient region, while in the low gradient region, fewer nodes can reduce the size of the data set without introducing too much error.
2) The boundaries of the materials must coincide with the boundaries of elements. This rule keeps the material property in each element constant.

Figure 3.1 shows a hexahedron element in local coordinates. Figure 3.2 (a) shows the geometry of a sample plate with a subsurface corrosion dome. Figure 3.2 (b) shows the FE mesh of the geometry.

The next step in developing a FE model is to choose an interpolation function, called shape function, to approximate the behavior of the unknown function within the element. Usually the polynomial function is used, since it is easy to differentiate and integrate. Also polynomials can approximate any arbitrary function if it contains enough terms. The linear

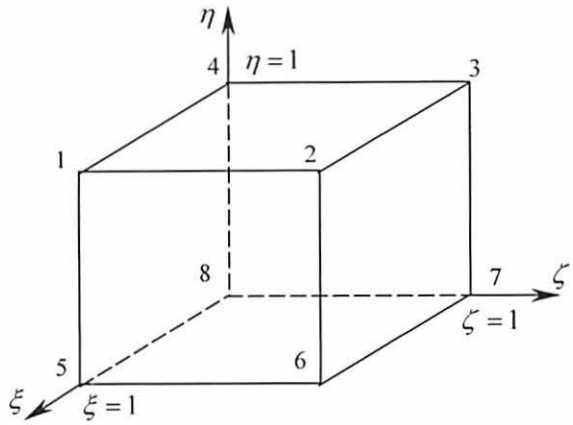

Figure 3.1 Hexahedral element in local coordinates.

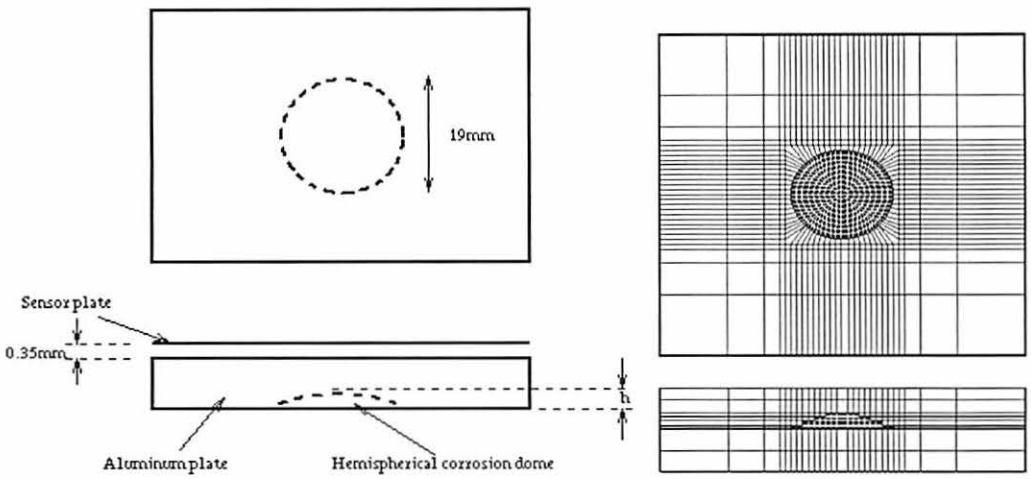

Figure 3.2 (a) A sample plate with corrosion dome (b) The top view and side view of the mesh. [13]

polynomial is used in this thesis because it is easy to implement and can achieve sufficient accuracy if the discretization is dense and elements are small.

The approximation functions for linear hexahedral elements can be defined in many ways. In order to evaluate the coefficients of the polynomial, the shape functions of different

elements are formulated in local coordinates. For example, for the element in Figure 3.1, the shape function for the *i*th node can be written as

$$N_i(\xi,\eta,\zeta) = c(1+\xi\xi_i)(1+\eta\eta_i)(1+\zeta\zeta_i)\,,\ \ i = 1,\ 2,\ \ldots,\ 8. \tag{3.22}$$

where the ξ, η, ζ are local coordinates of the elements

The shape function can be mapped onto global coordinates by using coordinate transformation. The relationships between local and global coordinates are

$$y = \sum_{i=1}^{8} N_i(\xi,\eta,\zeta) y_i \tag{3.24}$$

$$z = \sum_{i=1}^{8} N_i(\xi,\eta,\zeta) z_i\ . \tag{3.25}$$

Since we use linear hexahedral elements, the field function has the same formulation as the global coordinates *x*, *y*, and *z* and the magnetic vector potential in the element which can be written in terms of these nodal values as

$$A_x(x,y,z) = \sum_{i=1}^{8} N_i(\xi,\eta,\zeta) A_{xi} \tag{3.26}$$

$$A_y(x,y,z) = \sum_{i=1}^{8} N_i(\xi,\eta,\zeta) A_{yi} \tag{3.27}$$

$$A_z(x,y,z) = \sum_{i=1}^{8} N_i(\xi,\eta,\zeta) A_{zi} \tag{3.28}$$

The relationship between the shape functions derived in local coordinates and those derived in global coordinates is

$$\begin{bmatrix} \frac{\partial N_i}{\partial \xi} \\ \frac{\partial N_i}{\partial \eta} \\ \frac{\partial N_i}{\partial \zeta} \end{bmatrix} = \begin{bmatrix} \frac{\partial x}{\partial \xi} & \frac{\partial y}{\partial \xi} & \frac{\partial z}{\partial \xi} \\ \frac{\partial x}{\partial \eta} & \frac{\partial y}{\partial \eta} & \frac{\partial z}{\partial \eta} \\ \frac{\partial x}{\partial \zeta} & \frac{\partial y}{\partial \zeta} & \frac{\partial z}{\partial \zeta} \end{bmatrix} \begin{bmatrix} \frac{\partial N_i}{\partial x} \\ \frac{\partial N_i}{\partial y} \\ \frac{\partial N_i}{\partial z} \end{bmatrix} = [\mathbf{J}] \begin{bmatrix} \frac{\partial N_i}{\partial x} \\ \frac{\partial N_i}{\partial y} \\ \frac{\partial N_i}{\partial z} \end{bmatrix}, \tag{3.29}$$

where [J] is the Jacobian matrix. Then

$$\begin{bmatrix} \frac{\partial N_i}{\partial x} \\ \frac{\partial N_i}{\partial y} \\ \frac{\partial N_i}{\partial z} \end{bmatrix} = [\mathbf{J}]^{-1} \begin{bmatrix} \frac{\partial N_i}{\partial \xi} \\ \frac{\partial N_i}{\partial \eta} \\ \frac{\partial N_i}{\partial \zeta} \end{bmatrix}. \tag{3.30}$$

In the case of a volume integration one must replace the differential volume $dv=dxdydz$ with

$$dv = dxdydz = |\mathbf{J}| d\xi d\eta d\zeta \tag{3.31}$$

where $|\mathbf{J}|$ is the determinant of **J**.

3.4 Functional Minimization

As explained earlier, the energy functional must be minimized in the region of interest to achieve the energy balance in the solution region. This condition is satisfied by setting the partial derivates of $F(A)$ with respect to nodel values of **A** in each element to zero,

$$\frac{\partial F(A)}{\partial A_{ki}} = 0 \ , \quad i=1, 2, 3, \ldots, N; \quad k= x, y, z, \tag{3.32}$$

where N is the total number of nodes in the solution region. It is convenient to perform this procedure element by element, rather than in the entire solution region. In a linear hexahedral element, there are 8 nodes with three components A_x, A_y, A_z of **A**, the unknown magnetic vector potential, which results in 24 equations for each element. Substituting the

approximation functions of magnetic vector potential 3.23, 3.24, and 3.25 into Equation 3.32, we can get the following matrix equations for each element [22]:

$$\left[\begin{bmatrix} S_{3i-2,3j-2} & 0 & 0 \\ S_{3i-1,3j-2} & S_{3i-1,3j-1} & 0 \\ S_{3i,3j-2} & S_{3i,3j-1} & S_{3i,3j} \end{bmatrix} + j\omega\sigma \begin{bmatrix} R_{3i-2,3j-2} & 0 & 0 \\ 0 & R_{3i-1,3j-1} & 0 \\ 0 & 0 & R_{3i,3j} \end{bmatrix}\right]\begin{bmatrix} A_{xi} \\ A_{yi} \\ A_{zi} \end{bmatrix} = \begin{bmatrix} Q_{3i-2} \\ Q_{3i-1} \\ Q_{3i} \end{bmatrix}, \quad (3.33)$$

where the nonzero elements in the matrix equation are

$$S_{3i-2,3j-2} = \int_{vi}\left(\frac{\partial N_i}{\partial y}v\frac{\partial N_j}{z\partial y} + \frac{\partial N_i}{\partial z}v\frac{\partial N_j}{y\partial z}\right)dxdydz$$

$$S_{3i-1,3j-1} = \int_{vi}\left(\frac{\partial N_i}{\partial z}v\frac{\partial N_j}{x\partial z} + \frac{\partial N_i}{\partial x}v\frac{\partial N_j}{z\partial x}\right)dxdydz$$

$$S_{3i,3j} = \int_{vi}\left(\frac{\partial N_i}{\partial y}v\frac{\partial N_j}{x\partial y} + \frac{\partial N_i}{\partial x}v\frac{\partial N_j}{y\partial z}\right)dxdydz$$

$$S_{3i-1,3j-2} = -\int_{vi}\frac{\partial N_i}{\partial x}v\frac{\partial N_j}{z\partial y}dxdydz$$

$$S_{3i,3j-1} = -\int_{vi}\frac{\partial N_i}{\partial y}v\frac{\partial N_j}{x\partial z}dxdydz$$

$$S_{3i,3j-2} = -\int_{vi}\frac{\partial N_i}{\partial x}v\frac{\partial N_j}{y\partial z}dxdydz$$

$$R_{3i-2,3j-2} = R_{3i-1,3j-1} = R_{3i,3j} = \int_{vi}N_i dxdydz\ a$$

$$Q_{3i-2} = \int_{vi}J_x N_i dxdydz$$

$$Q_{3i-1} = \int_{vi}J_x N_i dxdydz$$

$$Q_{3i} = \int_{vi} J_x N_i dxdydz$$

where the $i, j = 1,2,3, \ldots, 8;$ and $v=\frac{1}{\mu}$. Solving these integrations using the Gaussian quadrature method, Equation 3.33 becomes a complex matrix equation

$$\{[S]+ j\omega\sigma[R]\}\{A\} = \{Q\}, \tag{3.34}$$

where the [S] is the real part of the 24×24 element matrix, [R] is the imaginary part of the 24×24 element matrix, [A] is 24×1 unknown magnetic potential vector, and [Q] is the 24×1 source vector.

The global matrix is the obtained by combining the individual element matrices. The value at each node is the sum of values contributed by all the connected elements. The global matrix equation is composed of 3×N simultaneous linear algebraic equations,

$$[G]\{A\} = \{Q\}, \tag{3.35}$$

where N is the total number of the nodes in the solution region. The global matrix,

$$[G] = [S]+ j\omega\sigma[R] \tag{3.36}$$

is of size 3N×3N complex non-symmetric and banded.

Since the matrix is also a sparse-banded matrix and the non-zero terms are clustered around the main diagonal, only the terms within the bandwidth of the upper and lower triangle matrices need to be stored. This is called bandwidth storage. There are also other storage methods used to store the stiffness matrix, such as skyline storage and non-zero elements storage.

3.5 Boundary Conditions

Boundary conditions should be specified before solving Equation 3.6. Either Dirichlet boundary conditions (the nodal values of **A** at boundary) or the Neumann boundary conditions (normal derivative of the function at boundary) can be specified. For the eddy current problem, the Neumann boundary conditions are implicit in the formulation and are satisfied automatically [22]. So we only need to impose the Dirichlet boundary conditions.

A simple method to impose Dirichlet boundary conditions is to use the 'blasting technique'. This technique involves multiplication of the diagonal element in the stiffness matrix corresponding to a boundary node by a large number, and the corresponding element in the {Q} vector replaced by a boundary value multiplied by the same large number. This will ensure that the off-diagonal terms in that row are neglected since they are very small compared to the diagonal element. Hence the boundary node is tied down to the boundary value specified.

3.6 Solution Methods of Finite Element Equations

The matrix Equation 3.38 can be solved by any standard solution technique. The solution methods of linear matrix equations are generally classified as direct methods and iterative methods. The Gaussian elimination method is a direct method used in this work to solve matrix equations and is used in this work along with bandwidth storage method of the system matrix.

Generally, the solution of the matrix equations takes more than 95% of the total computing time. Especially, when the geometry is complex and mesh is large, the stiffness matrix [G] for the mesh can use several gigabytes of memory, and the calculation may need

several days. In order to handle the huge computation, parallel computing was used [6]. This greatly increases the computing speed and allows calculation of more complex problems.

3.7 Post Processing

The solution of the matrix equation is in terms of the magnetic vector potential **A**. The magnetic vector potential **A** itself is not experimentally measurable, and therefore is of little value for comparison with measurements and other calculations [22].

The relation between the magnetic vector potential **A** and the flux density **B** is defined in Equation 3.9. It can be expanded to obtain components of **B** as

$$B_x = \frac{\partial A_z}{\partial y} - \frac{\partial A_y}{\partial z} \tag{3.40}$$

$$B_y = \frac{\partial A_x}{\partial z} - \frac{\partial A_z}{\partial x} \tag{3.41}$$

$$B_z = \frac{\partial A_y}{\partial x} - \frac{\partial A_x}{\partial y}. \tag{3.42}$$

For each element, the magnetic vector potential A at any point within the element varies linearly with respect to the nodal value A_i, where i= 1, 2, …, 8. This also implies that the flux density is invariant within the element. Substituting the nodal values of A in Equations 3.40 to 3.42, we can calculate the three component of the flux density in each element.

The eddy current density can also be calculated directly from the complex value of the magnetic vector potential as

$$J_{ex} = -j\omega\sigma A_x \tag{3.43}$$

$$J_{ey} = -j\omega\sigma A_y \tag{3.44}$$

$$J_{ez} = -j\omega\sigma A_z . \tag{3.45}$$

CHAPTER 4. RESULTS AND DISCUSSIONS

Finite element models are useful tools for studying the physics underlying the MOI phenomenon. The model serves as a test bed for generating signals from a variety of crack and corrosion geometries. The numerical results can also be used for optimizing parameters prior to the experiment. In this chapter, uses of the finite element model for various parametric studies are presented.

4.1 Geometry and Parameters of the Model

The schematic of the MOI device is shown is Figure 2.5. The purpose of the finite element modeling is to predict quantitative values of the leakage magnetic field at the MO sensor due to eddy currents induced in the test specimen. Since this is a localized phenomenon, symmetry of the geometry and appropriate boundary conditions are used to minimize the complexity of modeling without losing accuracy.

The MO sensor consists of multiple layers as shown is Figure 4.1. The copper foil in the sensor carries the excitation sheet current. There are layers of fiberglass and a wear pad between the copper foil and the specimen, which have a total thickness of 0.35mm.

In a numerical model, the test sample is an aluminum plate of 1.25mm thickness. A current inducing foil of 0.04mm thickness is placed above the aluminum sample plate at a distance of 0.35mm. A circular hole with a radius of 4mm is introduced in the plate as shown in Figure 4.2. The parameter values used in the numerical model are summarized in Table 4.1. The induced magnetic field (B_Z) is computed in the sensor substrate which is 0.5mm thick and directly above the current inducing foil.

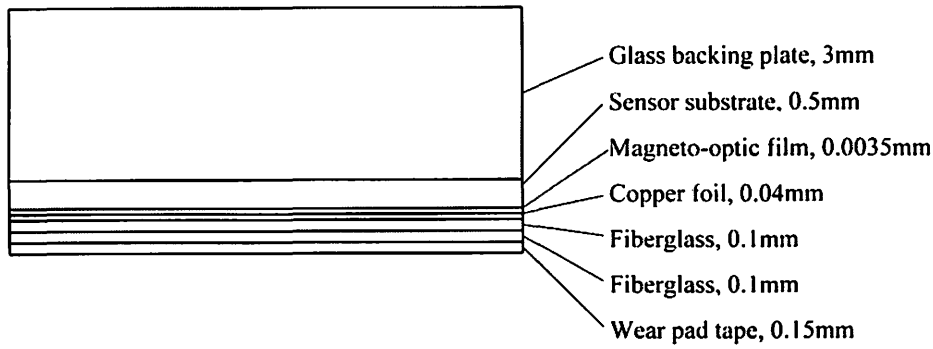

Figure 4.1 MO sensor configuration showing total spacing between the magneto-optic film and the specimen.

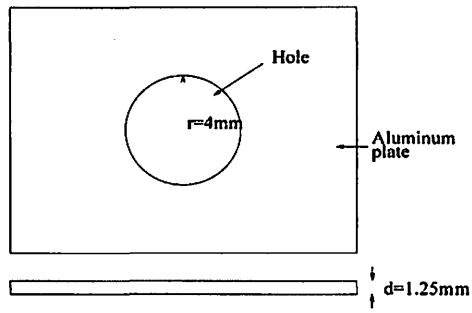

Figure 4.2 Test geometry

Table 4.1. Parameters used in the finite element model.

Parameter	Value
Frequency	3 KHz
Source current density(J_s)	10^8 A/m
Copper foil conductivity (σ_f)	5.8001×10^7 S/m
Aluminum conductivity (σ_{AL})	1.8867×10^7 S/m

Figure 4.3 shows the region of interest modeled using the finite element method. One quarter of the region is discretized into small elements using symmetry of the geometry. The boundary conditions applied on the six boundary faces are summarized as follows:

S_{1234} (top) $A_X = 0, \quad A_Y = 0, \quad A_Z = 0;$

S_{5678} (bottom) $A_X = 0, \quad A_Y = 0, \quad A_Z = 0;$

S_{1265} (front) $A_X = 0, \quad \partial A_Y/\partial n = 0, \quad A_Z = 0;$

S_{4378} (rear) $A_X = 0, \quad \partial A_Y/\partial n = 0, \quad A_Z = 0;$

S_{1485} (left) $A_X = 0, \quad \partial A_Y/\partial n = 0, \quad A_Z = 0;$

S_{2376} (right) $A_X = 0, \quad \partial A_Y/\partial n = 0, \quad A_Z = 0.$

Figure 4.4 shows the discretization and the source currents in the plane $x = 0.35mm$. The finite element mesh includes a hole in the aluminum plate can be seen in Figure 4.5 [6].

4.2 Validation of the Model

The model was validated by comparing the numerically computed magneto-optic images with the experimental images qualitatively and quantitatively. An aluminum plate with a circular hole, shown in Figure 4.2, was modeled using the mesh shown in Figure 4.5. This mesh has 1573 elements and 2016 nodes. The magnetic flux density (B_Z) in the sensor substrate computed by the model is plotted in Figure 4.6. Figures 4.7 (a) and (b) present the measured and model predicted MO images for this geometry. Note that the x-y scales on the two images are not the same; however, their shapes are similar and the corresponding peak values $\overset{\rho}{B}_{z\max}$ are around 6 Gauss in both cases. Figure 4.8 shows the distribution of induced eddy currents in an aluminum plate without any defects.

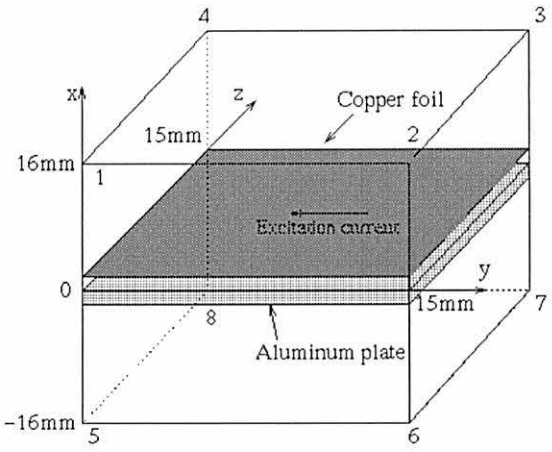

Figure 4.3 Single layer aircraft geometry with current inducing foil.

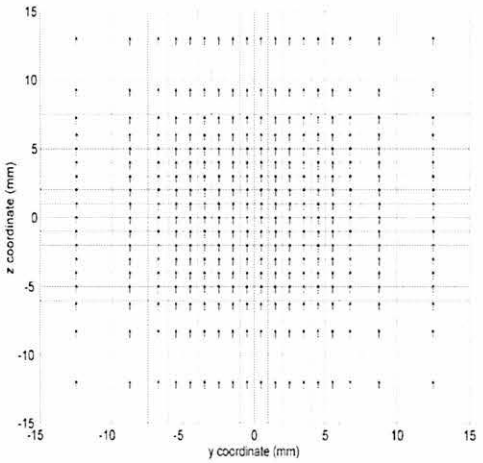

Figure 4.4 Source current in the copper foil as described by the mesh.

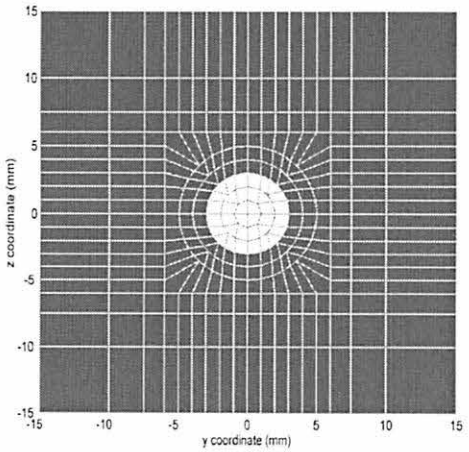

Figure 4.5 Top view of the mesh of aluminum plate with circular hole

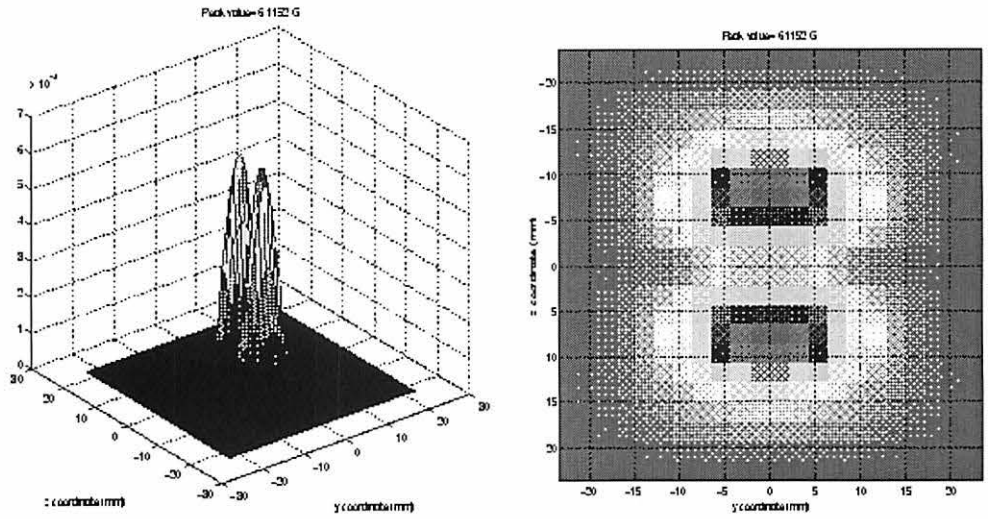

Figure 4.6 Magnetic field B_Z in the sensor substrate.

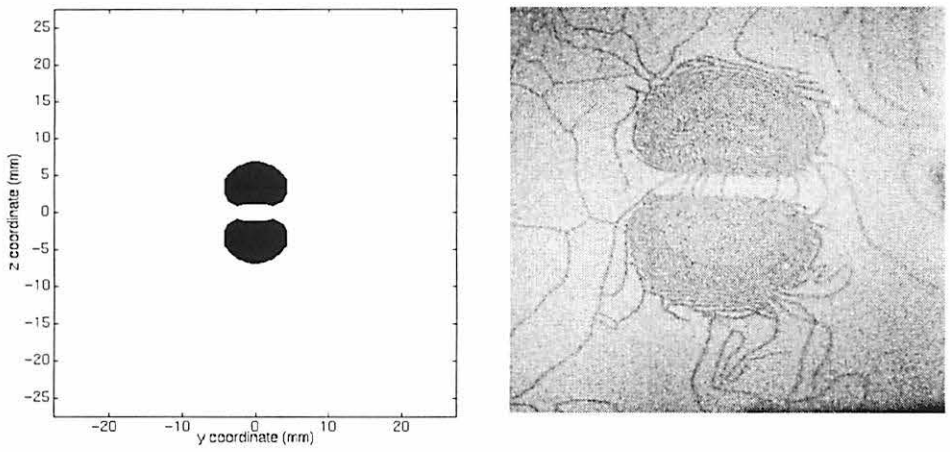

(a) (b)

Figure 4.7 Magnetic field B_Z in the sensor substrate due to a circular hole in an aluminum plate at frequency of 3 kHz. (a) model prediction and (b) experimental measurement.

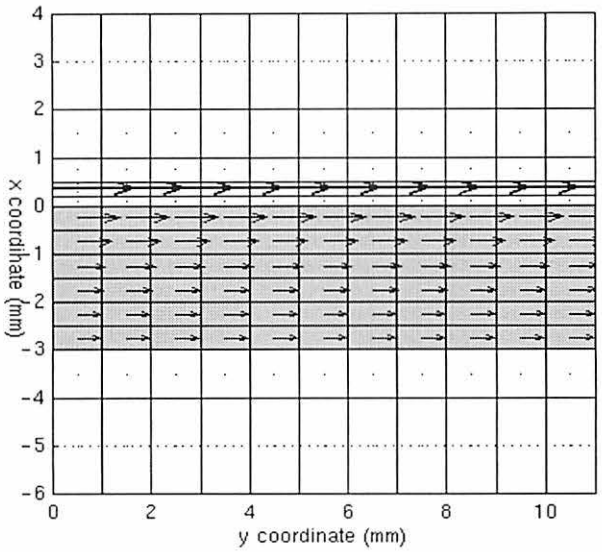

Figure 4.8 The distribution of induced eddy currents in an aluminum plate without any defects.

4.3 Effect of the Depth of the Corrosion Dome

Figure 4.9 shows the cross-section of the geometry of a subsurface corrosion dome. The test sample is an aluminum plate of 1.5mm thickness. A corrosion pit in the form of a hemispherical dome of 19mm diameter and height h mm is introduced in the plate as shown in Figure 4.9. Figure 4.10 shows the region of interest in the y-z and z-x plane discretized using a finite element mesh (with 7514 elements and 8748 nodes). The parameter values used in the numerical model are summarized in Table 4.1. Due to induced eddy currents, a magnetic field (B_Z) is generated in the sensor substrate which is 0.5mm thick and directly above the current-inducing foil. The model computes the induced eddy currents in the sample and the resulting magnetic flux in the sensor.

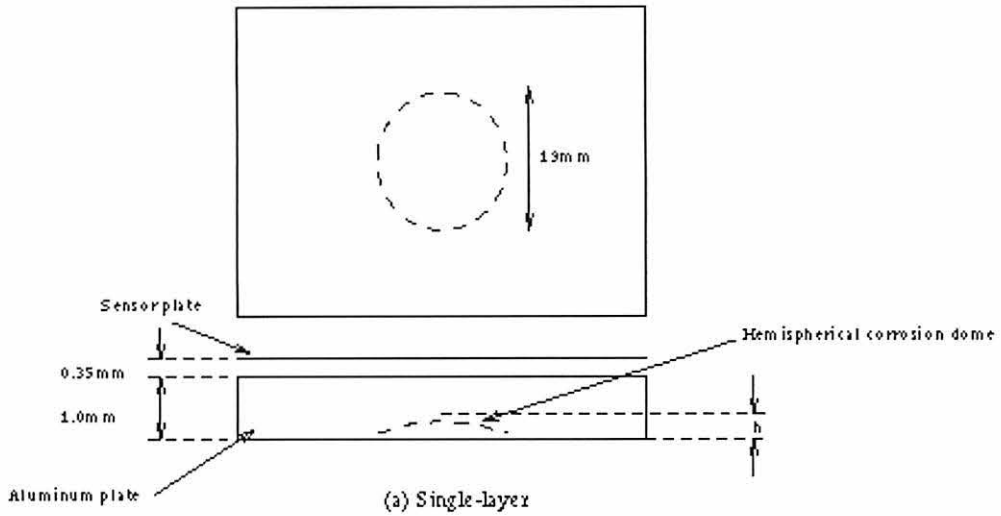

Figure 4.9 Geometry of single layer sample plate

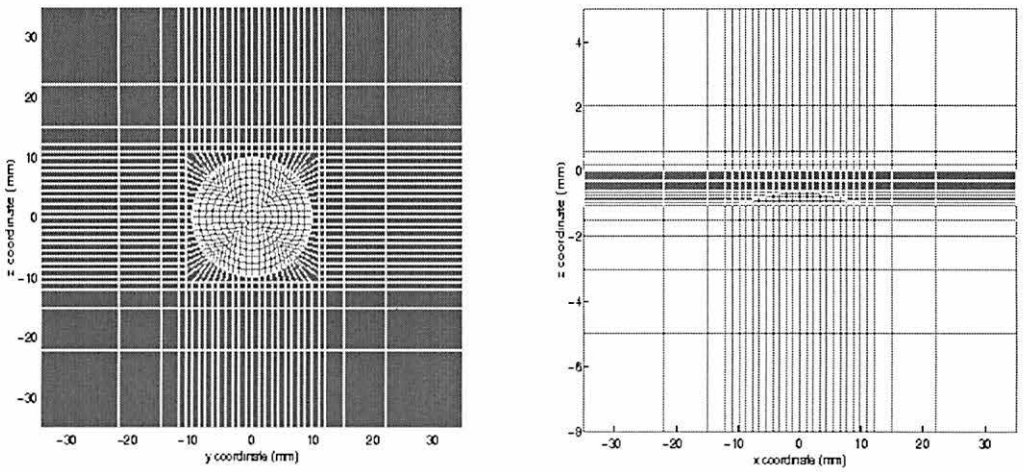

(a) (b)

Figure 4.10 Discretization used in finite element mesh as seen in the *y-z* (a) and *z-x* (b) plane.

The distributions of B_z in sensor for 10%, 20%, 30%, 40% corrosion domes in the single layer geometry are shown in Figures 4.11 through 4.13 as both surface plots (a) and intensity

plots (b). From these results, we find the peak values of the flux leakage increase with the depth of the corrosion dome, which agree with the experimental results.

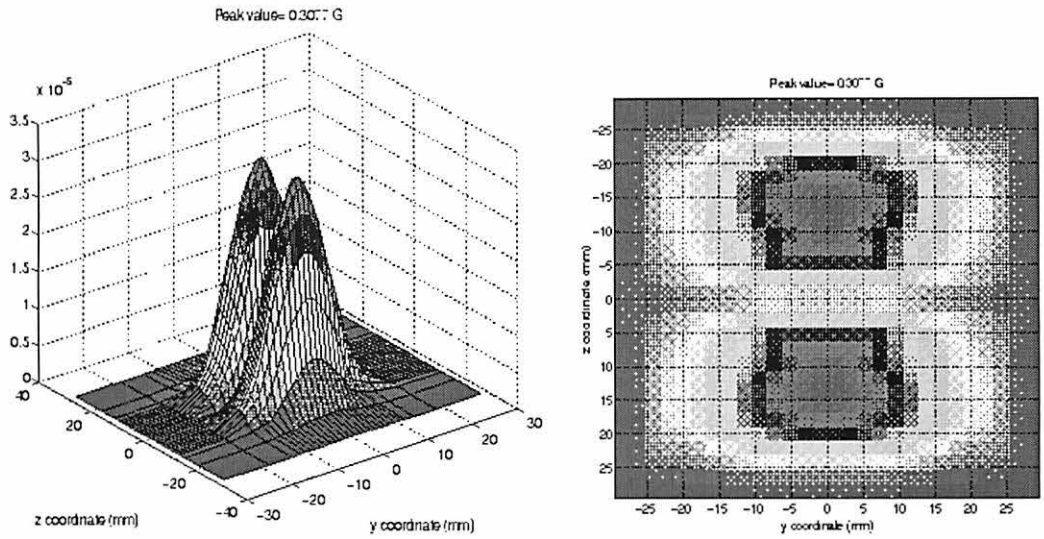

(a) (b)

Figure 4.11 (a) Surface plot and (b) image of B_Z in the sensor substrate for 10% corrosion dome in single layer geometry.

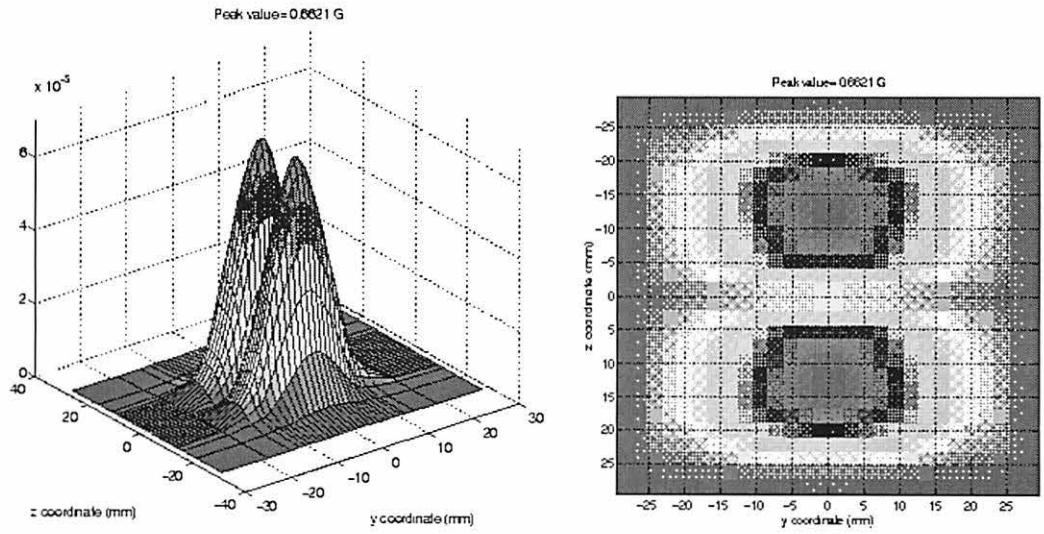

(a) (b)

Figure 4.12 (a) Surface plot and (b) image of B_Z in the sensor substrate for 20% corrosion dome in single layer geometry.

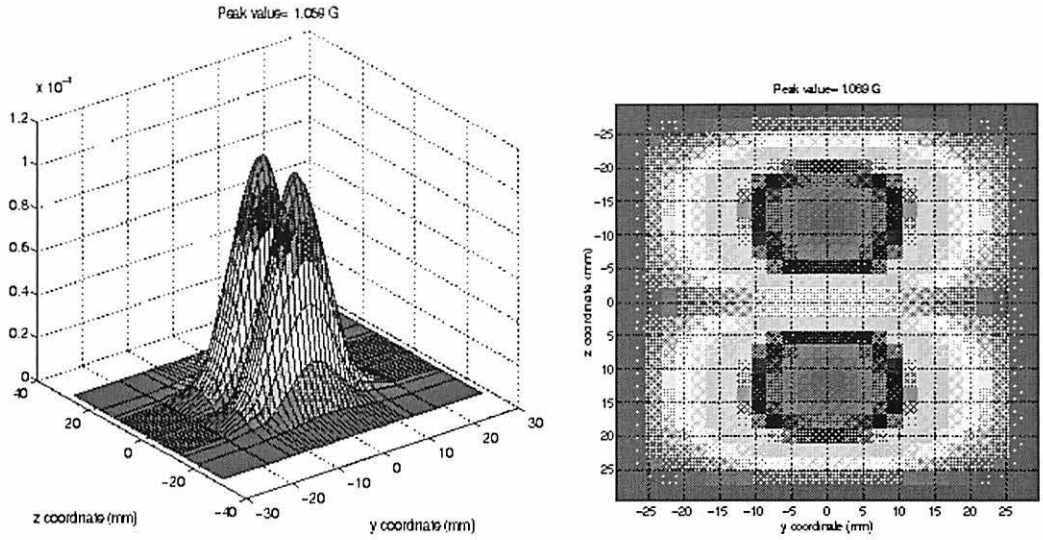

(a) (b)

Figure 4.13 (a) Surface plot and (b) image of B_Z in the sensor substrate for 30% corrosion dome in single layer geometry.

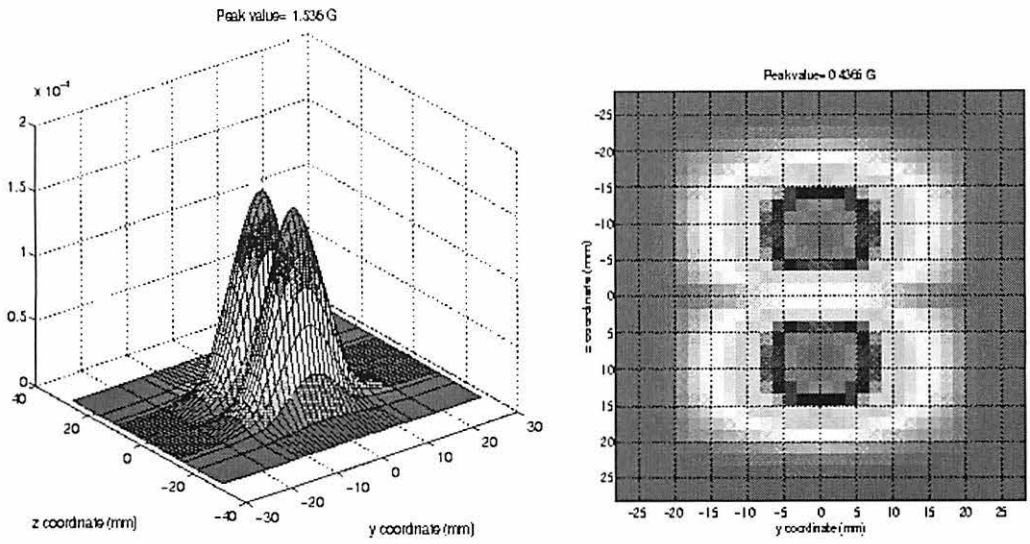

(a) (b)

Figure 4.14 (a) Surface plot and (b) image of B_Z in the sensor substrate for 40% corrosion dome in single layer geometry.

4.4 Effect of Second Layer on Corrosion

The model was then modified to study the effect of a second layer of aluminum in the geometry below the first layer. The geometry is shown in Figure 4.15. Figure 4.10 shows the region of interest in the *y-z* and *z-x* plane discretized using a finite element mesh.

The presence of a second layer of aluminum below the corrosion, provides an additional path for the induced eddy currents, thereby reducing the magnetic flux at the sensor placed above the first plate. The peak values of magnetic field in the presence of the second layer is, therefore, reduced by a factor of 2. The distributions of B_Z in the sensor for 10%, 20%, 30%, 40% corrosion domes in the presence of the second layer are shown in Figure 4.16 through 4.19 as both surface plots (a) and intensity plots (b).

Figure 4.20 shows that peak amplitudes of the magnetic field $\overset{\rho}{B}_{z\max}$ as a function of height *h* of the corrosion dome for both single and double layer geometry.

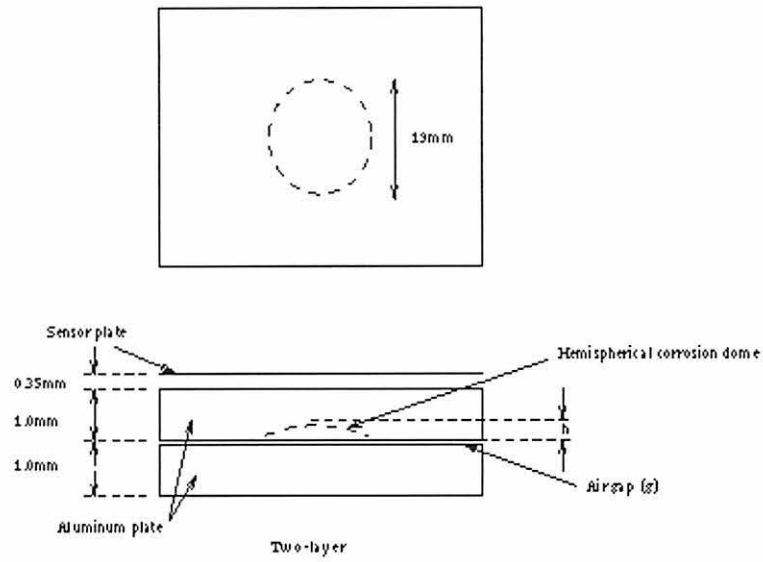

Figure 4.15 Geometry of two layer sample plate with corrosion dome in the bottom upper layer.

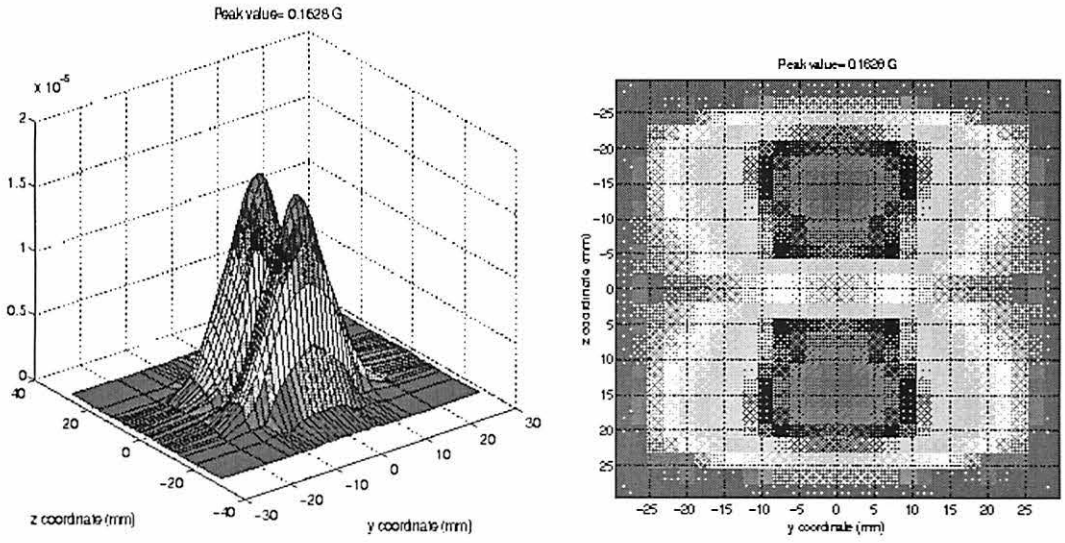

(a) (b)

Figure 4.16 (a) Surface plot and (b) image of B_z in the sensor substrate for 10% corrosion dome in the bottom of the upper layer.

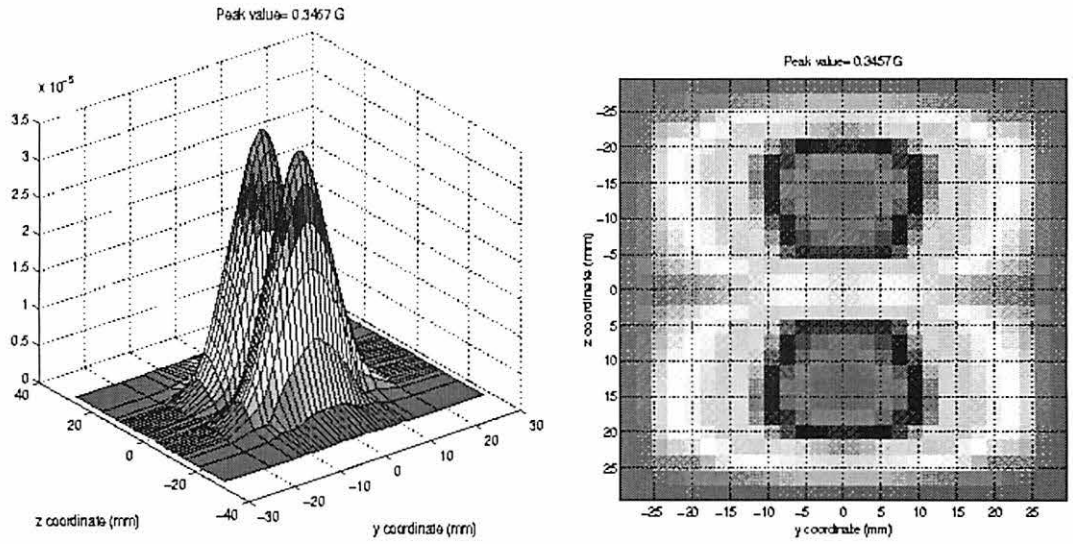

(a) (b)

Figure 4.17 (a) Surface plot and (b) image of B_Z in the sensor substrate for 20% corrosion dome in the bottom of the upper layer.

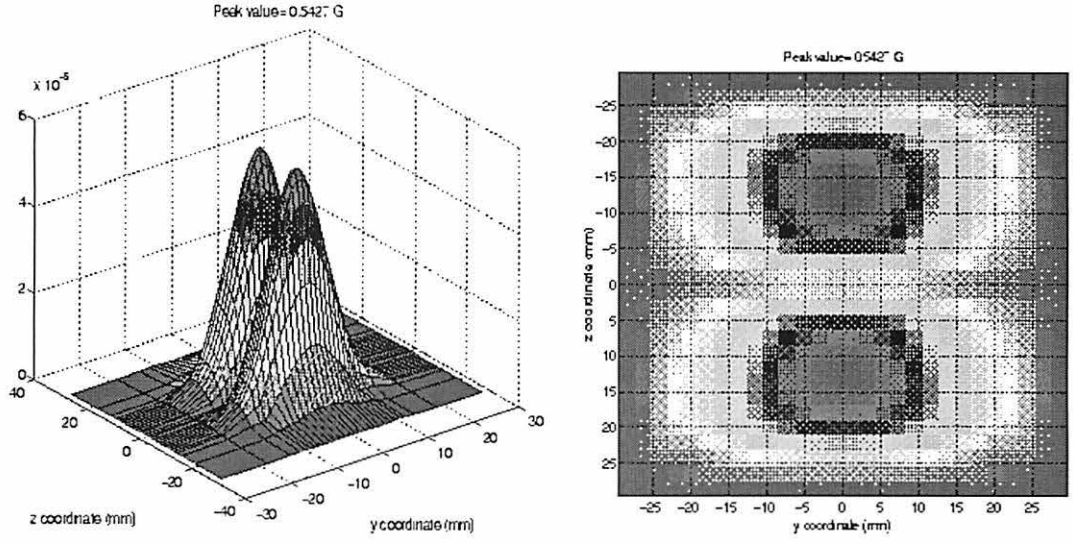

(a) (b)

Figure 4.18 (a) Surface plot and (b) image of B_Z in the sensor substrate for 30% corrosion dome in the bottom of the upper layer.

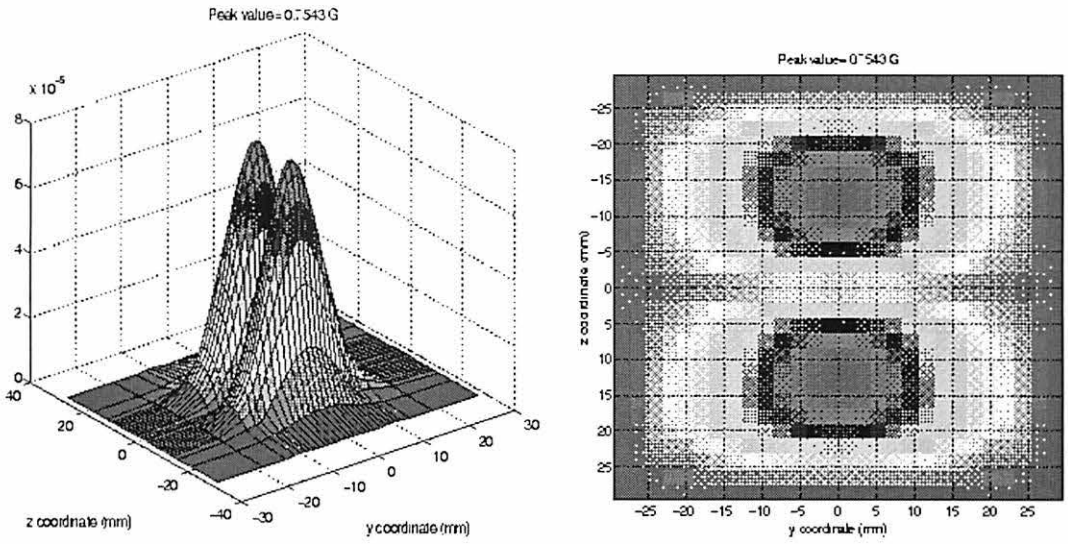

(a) (b)

Figure 4.19 (a) Surface plot and (b) image of B_Z in the sensor substrate for 40% corrosion dome in the bottom of the upper layer.

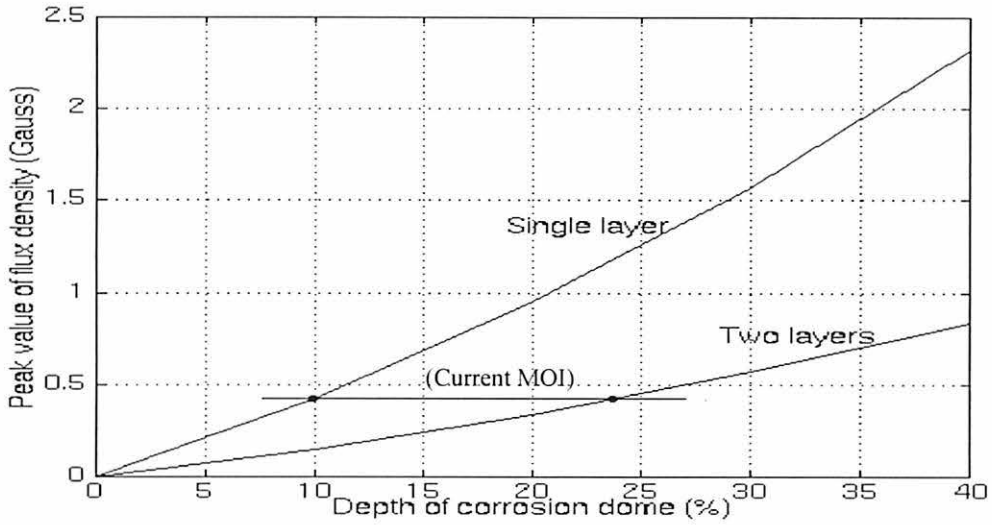

Figure. 4.20 Peak value of magnetic flux density as a function of corrosion dome height for the single and two layer geometry.

The FEM results are consistent with experimental observations in that the presence of a second layer skin reduces the fields at the surface by a factor of two. The experimental MOI observations show that a 10% dome is detectable in a single layer, whereas, with two layers such as in lap joint, only 20% corrosion loss is detectable by MOI instrument. The calculations illustrated in Figure 4.20 provide an important guide to the required MO developments as a function of the required defect-detection capability.

4.5 Effect of Excitation Frequency

This section presents the results obtained at various excitation frequencies. The single and double layer geometry used in this section are same as the geometry shown in Figure 4.9 and 4.14, respectively. The corrosion depth is kept fixed at 20%. The parameter values used in the numerical model are summarized in Table 4.1, except that the excitation frequency was varied from 500Hz to 5000Hz.

The excitation frequency will affect the skin depth of the eddy current, and hence affect the magnetic flux density generated by different corrosion depths. Figure 4.21 shows the peak value of magnetic flux density as a function of excitation frequency for both single layer sample with corrosion dome and two-layer sample with corrosion dome in the second layer. It was found that the optimum frequency for detecting the corrosion dome in a single layer sample is 1kHz, whereas, for detecting the corrosion dome in the presence of the second layer sample, the optimum frequency is reduced to 0.5kHz.

This study was exploited to investigate the changes in the corresponding MOI images generated at the different frequencies. It was felt that the evolution of the images with frequencies would provide valuable information for defect characterization. Contours of the

image obtained using a threshold of 0.1 Gauss are shown in Figure 4.22.

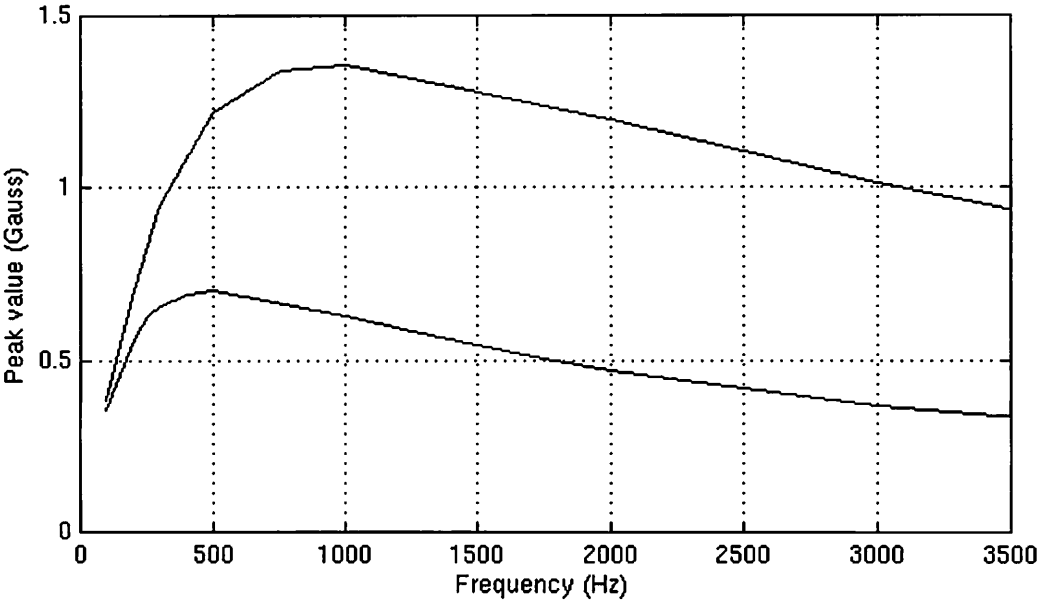

Figure 4.21 Peak value of magnetic flux density as a function of excitation frequency for both (a) single layer sample with corrosion dome and (b) two-layer sample with corrosion dome in the second layer.

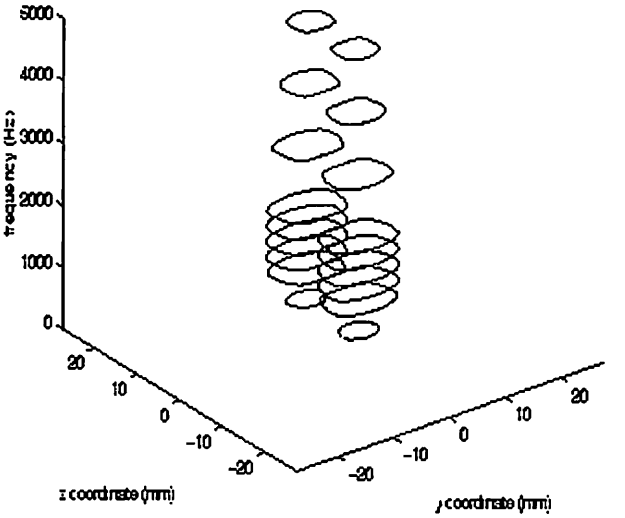

Figure 4.22 Contours of the images predict by the model changes with the frequency for 20% corrosion dome depths in first layer.

4.6 Effect of Corrosion Dome on Top of the Second Layer

Usually, corrosion occurs between different layers. We have modeled the corrosion in the bottom of the first layer. In order to study the effect of corrosion location, the corrosion dome on the top of the second layer was modeled. Figure 4.23 shows the geometry of two layer samples with the corrosion dome at the top of the second layer.

Four corrosion depths namely, 10%, 20%, 30% and 40% of the thickness of one layer were modeled. The air gap between the two layers is chosen to be 0mm, which means the two layers are connected as one conductor. The case when the air gap is not zero is studied in the following section. The parameter values used in this model are the same as those in Table 4.1, except that the excitation frequency is 1.5kHz.

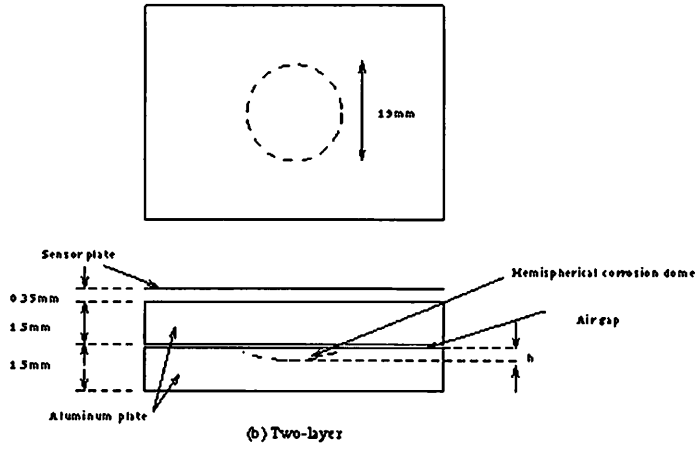

Figure 4.23 The geometry of two layer sample with corrosion dome on top of the second layer.

The normal component of the flux density was computed for each of the four corrosion depths. The results are shown in Figures 4.24 through 4.27 as both surface plots (a) and intensity plots (b). Figure 4.28 shows the peak value of magnetic flux density as a function of corrosion depth for corrosion at both the bottom of the first layer and the top of the second layer.

For the same corrosion depth, the peak value of the flux leakage for the corrosion at the top of the second layer is smaller than that of the corrosion at the bottom of the first layer. Also, comparing Figure 4.24 through 4.27 with Figures 4.16 through 4.19, we find the distribution of the fields for these two conditions are different. This information can be useful for defect characterization, and estimating defect location.

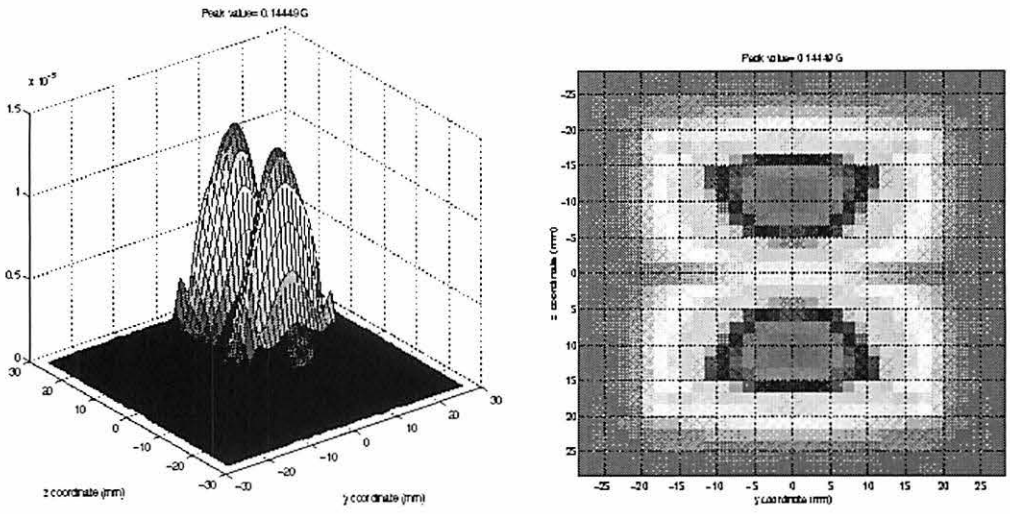

(a) (b)

Figure 4.24 (a) Surface plot and (b) image of B_Z in the sensor substrate for 10% corrosion dome in the top of the second layer.

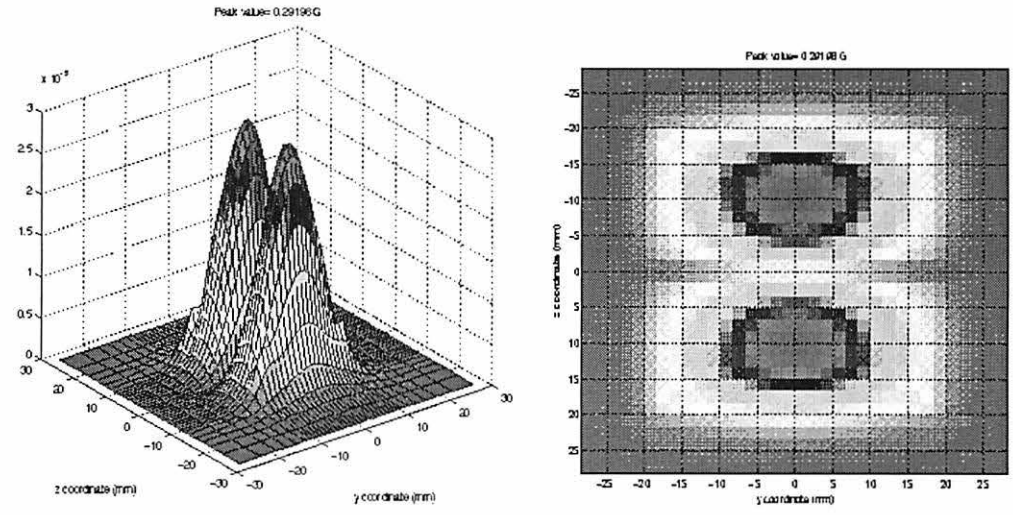

(a) (b)

Figure 4.25 (a) Surface plot and (b) image of B_Z in the sensor substrate for 20% corrosion dome in the top of the second layer.

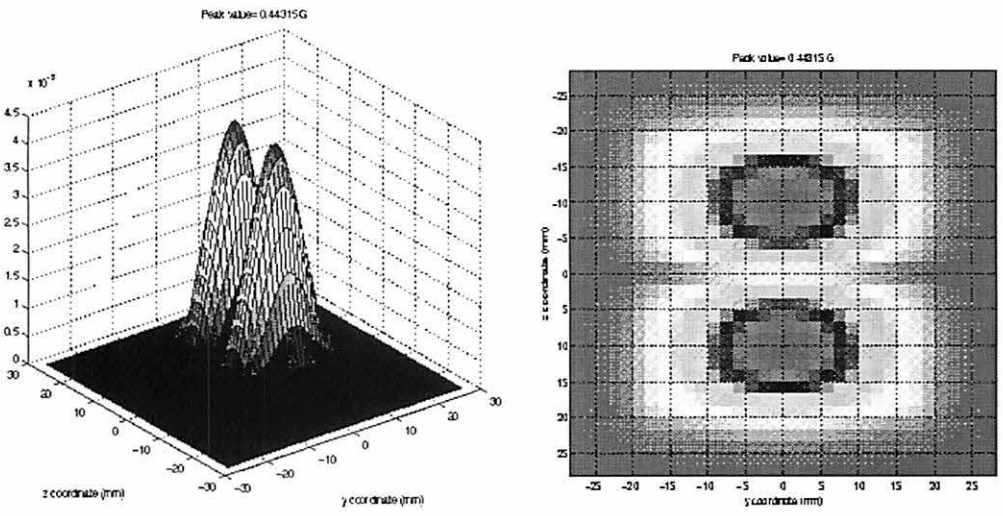

(a) (b)

Figure 4.26 (a) Surface plot and (b) image of B_Z in the sensor substrate for 30% corrosion dome in the top of the second layer.

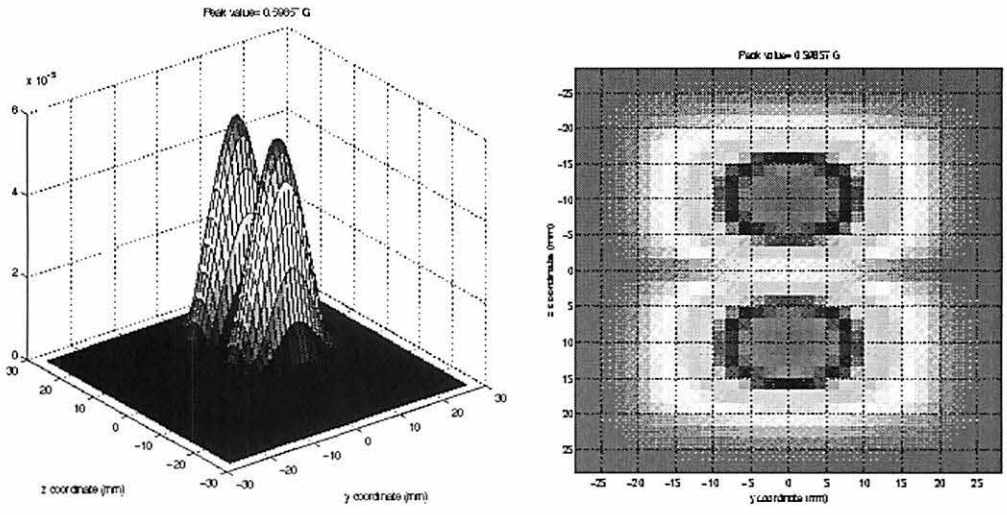

(a) (b)

Figure 4.27 (a) Surface plot and (b) image of B_Z in the sensor substrate for 40% corrosion dome in the top of the second layer.

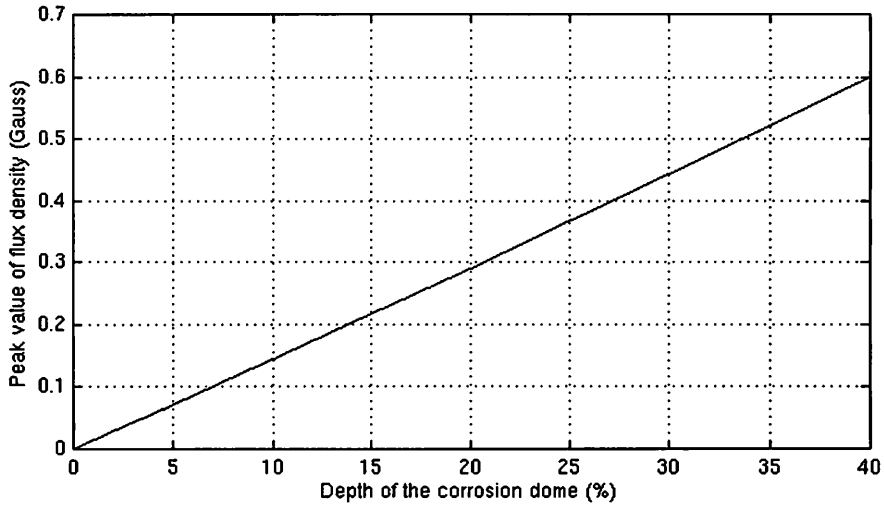

Figure 4.28 Peak value of magnetic flux density as a function of corrosion depth for corrosion on the top of the second layer.

4.7 Effect of the Air Gap between layers

In practice, air gaps exist between different layers of the aircraft skin. This section presents the results obtained at various values of the air gap between the two layers. The corrosion dome depth is kept fixed at 20%. The effect of the air gap was studied with the corrosion dome introduced at (1) bottom of the first layer and (2) top of the second layer. The geometry is shown in Figure 4.19. The air gap values chosen are 0mm, 0.5mm and 1mm and the test was carried out at 1.5kHz frequency.

Figure 4.29 shows the variation of the peak value of B_Z versus the air gap for corrosion dome in the first layer and the second layer at a frequency of 1.5kHz. It apparent that when the corrosion is in the first layer, increase in air gap results in an increase in the peak value of B_Z tending to the single layer value, whereas when the corrosion is in the second layer, the field becomes weaker at larger air gaps, due to larger liftoff.

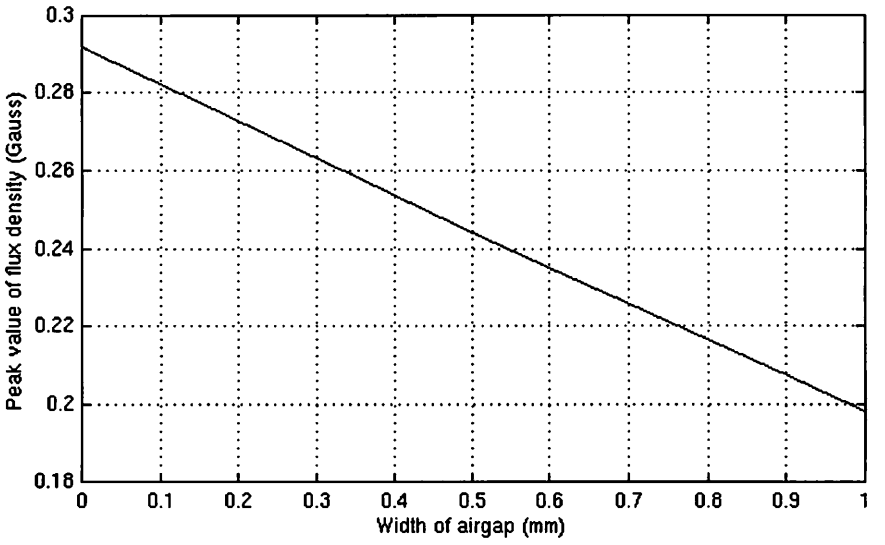

Figure 4.29 Peak value of B_Z versus the air gap.

4.8 Effect of the Slope of the Corrosion Domes

In a practical situation, the shapes of actual corrosion can be complex. In this section, we investigated the effect of corrosion dome slopes on the images produced by the sensor.

The FE model predicts the normal component of the magnetic flux density, which will be detected by a Magneto-Optic sensor due to the different slopes of the corrosion dome. The geometry used in the numerical model is similar to the geometry shown in Figure 4.9. The difference is that the slope of the corrosion dome is varied; thus the diameter of the corrosion dome is not always 19mm.

The parameter used in this section is the same as those listed in Table 4.1.

The side view of the sample plates and the corresponding normal component of flux density are presented in Figures 4.31 to 4.37.

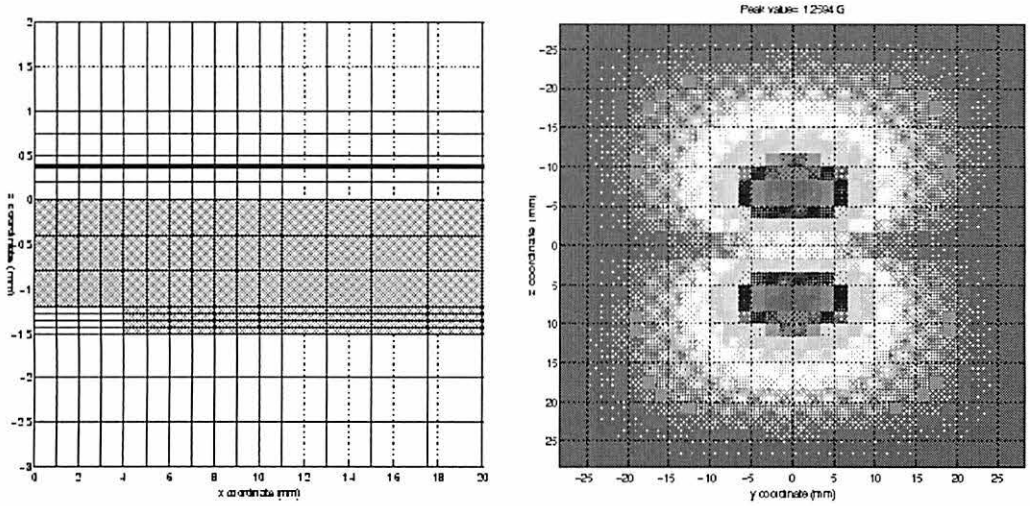

(a) (b)

Figure 4.31 (a) The X-Z side view of the sample plate; (b) image of B_Z in the sensor substrate for a 20% corrosion dome at a frequency of 3kHz.

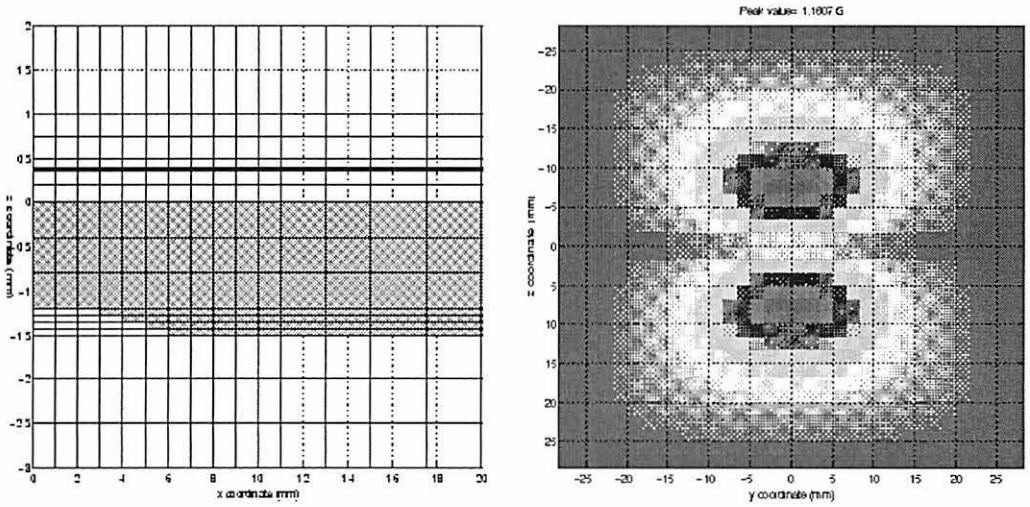

(a) (b)

Figure 4.32 (a) The X-Z side view of the sample plate; (b) image of B_Z in the sensor substrate for a 20% corrosion dome at a frequency of 3kHz.

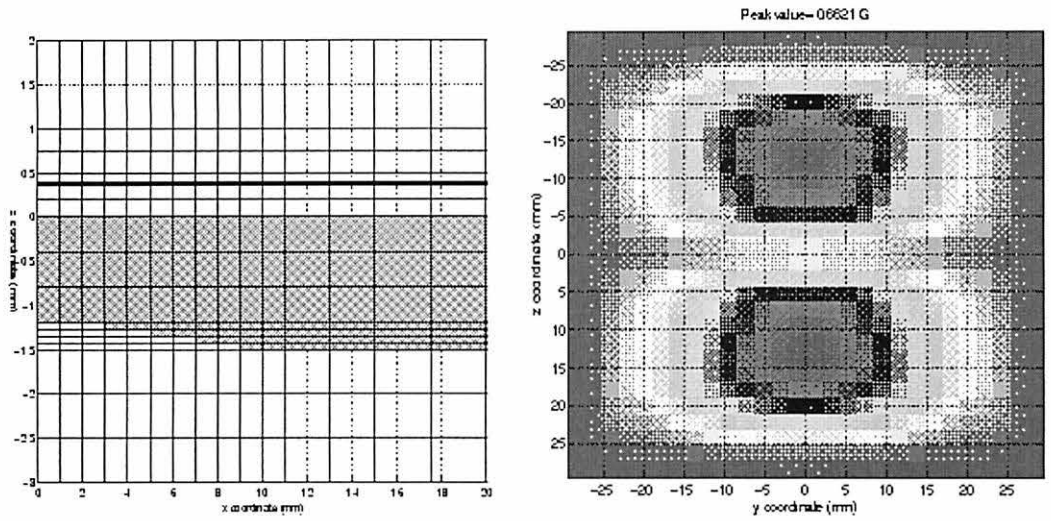

(a) (b)

Figure 4.33 (a) The X-Z side view of the sample plate; (b) image of B_Z in the sensor substrate for a 20% corrosion dome at a frequency of 3kHz.

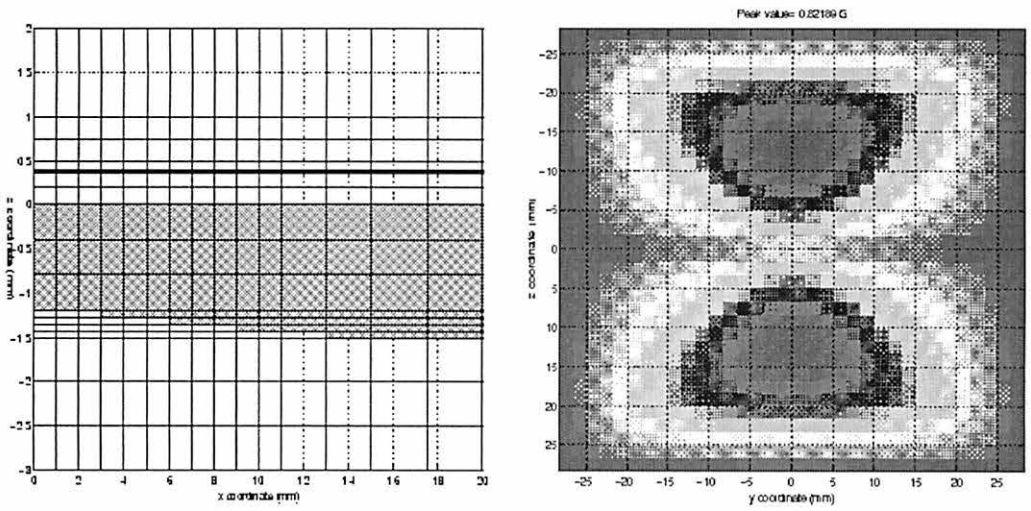

(a) (b)

Figure 4.34 (a) The X-Z side view of the sample plate; (b) image of B_Z in the sensor substrate for a 20% corrosion dome at frequency of 3kHz.

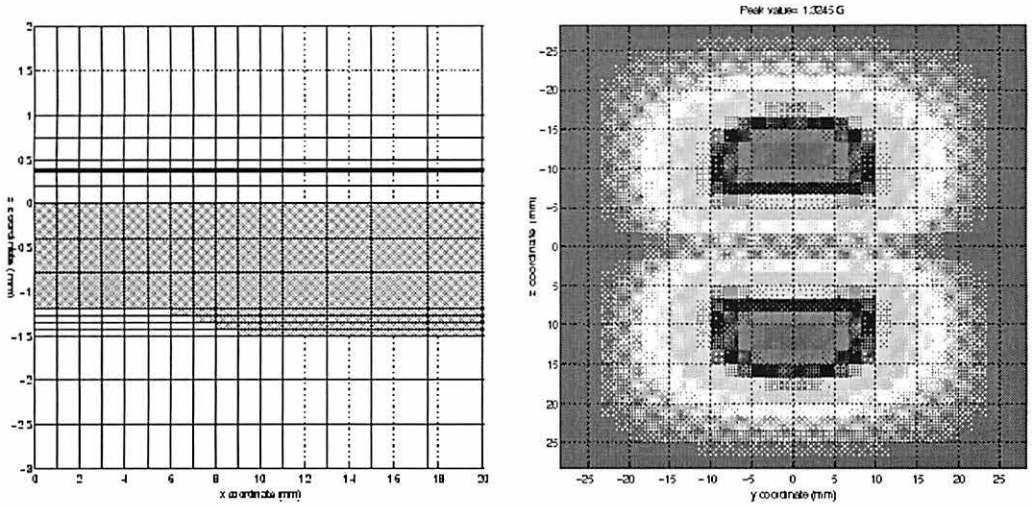

(a) (b)

Figure 4.35 (a) The X-Z side view of the sample plate; (b) image of B_Z in the sensor substrate for a 20% corrosion dome at a frequency of 3kHz.

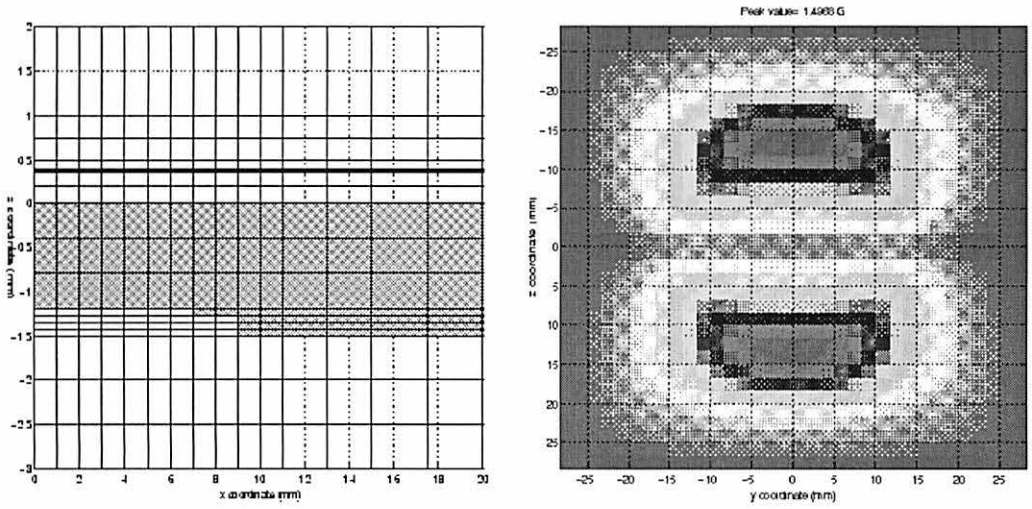

(a) (b)

Figure 4.36 (a) The X-Z side view of the sample plate; (b) image of B_Z in the sensor substrate for a 20% corrosion dome at a frequency of 3kHz.

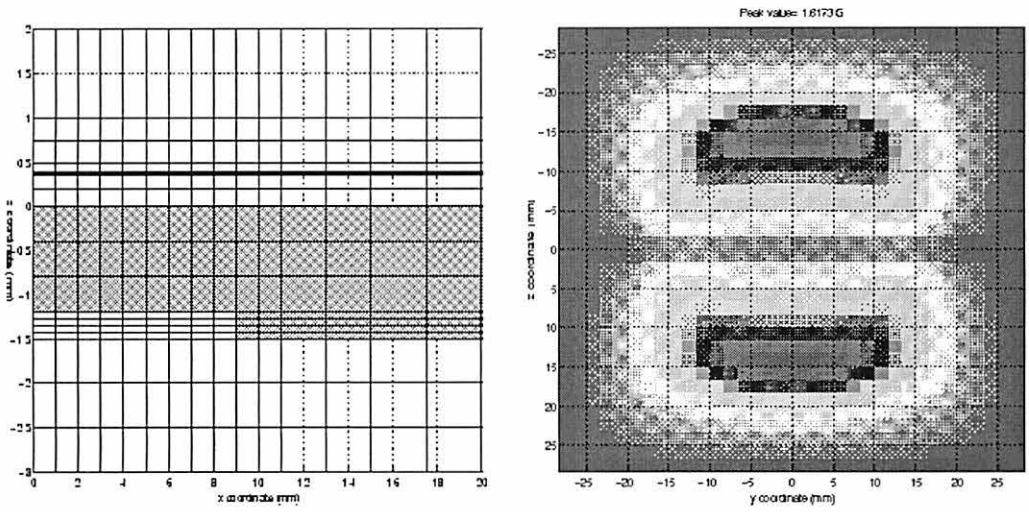

(a) (b)

Figure 4.37 (a) The X-Z side view of the sample plate; (b) image of B_Z in the sensor substrate for a 20% corrosion dome at a frequency of 3kHz.

From the above figures, we find that when the slope increases, the normal component of the peak value of magnetic flux density becomes larger. Also, we notice that the shape of the flux leakage image is distinctly different, as corrosion goes from a straight edge to a dome shape. This information is again useful for defect characterization purpose.

CHAPTER 5. CONCLUSIONS AND FUTURE WORK

5.1 Summary and Conclusions

The magneto-optic/eddy current method is a relatively new and promising NDT method in aircraft inspection. The MOI has gained increased popularity largely due to its distinct advantages. MOI can detect much deeper defects than the traditional eddy current method. The large area coverage and the real time image of the specimen make the inspection easy and fast. The MO image is easy to interpret, which in turn saves training time for operators.

The challenge of detecting deeper, smaller, and more complex defects makes it necessary to continually improve the sensitivity of sensor and instrument design. The key to the instrument's capability in detecting the relatively weak magnetic fields associated with subsurface defects is the sensitivity of the MO sensor. The finite element model simulating the magneto-optic imaging process helps in obtaining a quantitative estimate of the improvement needed.

This thesis describes the development of a finite element model for predicting quantitative values of the fields under different parametric conditions. The effect of various parameters on the magnetic flux leakage, such as depth of the corrosion dome, excitation frequency, multi-layer sample plate, air gap between sample plates, and slope of the corrosion dome have been studied. The FE model simulates the influence of the parameters on the magnetic flux leakage and predicts the output MO images. The model predicted images are also useful in inferring information regarding shape of the underlying defects. The results of this thesis have clearly demonstrated the usefulness of the simulation models in

visualizing the flux distribution, design optimization, defect characterizations, and parametric studies.

5.2 Future Work

Results obtained so far compare very well with experimental observation. One of the future tasks is to address the problem of modeling the CUF geometry as shown in Figure 1.6. In order to handle these important problems of interest to industry, more efficient storage methods and a faster solver to solve the global matrix equation is very necessary. The non-zero element storage and conjugate gradient method are also being developed.

The finite element method we used in this work is node-based, i.e., the unknown parameters are assigned to nodes of elements. This formulation however gives rise to spurious solutions particularly at the boundary between two materials with different permittivity or permeability. Nodal formulation enforces continuity of the unknown values across elements and it is difficult to express the discontinuity of normal components of the **E** and **H** fields. Edge elements are finite elements whose degrees of freedom are assigned to edges rather than nodes. This formulation allows us to enforce tangential continuity and allow normal discontinuity along the boundary. Edge element formulation for MOI applications is in progress.

Another aspect of MOI inspection is the interpretation and classification of resulting MO images. Automated image processing and classification algorithms can help in interpretation of data. The FE model can be used to predict the field images for various defect shapes. Using image processing techniques and neural network based algorithms, a reliable image

interpretation algorithm can be developed. This image interpretation technique will increase the speed and sensitivity of the MOI instrument.